




# eROSITA studies of the Carina nebula

Manami Sasaki<sup>1</sup> , Jan Robrade<sup>2</sup> , Martin G. H. Krause<sup>3</sup>, Jonathan R. Knies<sup>1</sup>, Kisetu Tsuge<sup>1</sup>,  
Gerd Pühlhofer<sup>4</sup> , and Andrew Strong<sup>5</sup>

<sup>1</sup> Dr. Karl Remeis Observatory, Erlangen Centre for Astroparticle Physics, Friedrich-Alexander-Universität Erlangen-Nürnberg, Sternwartstraße 7, 96049 Bamberg, Germany  
e-mail: manami.sasaki@fau.de

<sup>2</sup> Hamburger Sternwarte, Universität Hamburg, Gojenbergsweg 112, 21029 Hamburg, Germany

<sup>3</sup> Centre for Astrophysics Research, School of Physics, Astronomy and Mathematics, University of Hertfordshire, College Lane, Hatfield, Hertfordshire AL10 9AB, UK

<sup>4</sup> Institut für Astronomie und Astrophysik, Universität Tübingen, Sand 1, 72076 Tübingen, Germany

<sup>5</sup> Max-Planck-Institut für extraterrestrische Physik, Gießenbachstraße 1, 85748 Garching, Germany

Received 11 June 2023 / Accepted 3 December 2023

## ABSTRACT

**Context.** During the first four all-sky surveys eRASS:4, which was carried out from December 2019 to 2021, the extended Roentgen Survey with an Imaging Telescope Array (eROSITA) on board the Spektrum-Roentgen-Gamma (Spektr-RG, SRG) observed the Galactic H II region, the Carina nebula.

**Aims.** We analysed the eRASS:4 data to study the distribution and spectral properties of the hot interstellar plasma and the bright stellar sources in the Carina nebula.

**Methods.** The spectral extraction regions of the diffuse emission were defined based on the X-ray spectral morphology and multi-wavelength data. The spectra were fit with a combination of thermal and non-thermal emission models. The X-ray bright point sources in the Carina nebula are the colliding wind binary  $\eta$  Car, several O stars, and Wolf-Rayet (WR) stars. We extracted the spectra of the brightest stellar sources, which can be well fit with a multi-component thermal plasma model.

**Results.** The spectra of the diffuse emission in the brighter parts of the Carina nebula are well reproduced by two thermal models, a lower-temperature component ( $\sim 0.2$  keV) and a higher-temperature component (0.6–0.8 keV). An additional non-thermal component dominates the emission above  $\sim 1$  keV in the Central region around  $\eta$  Car and the other massive stars. Significant orbital variation in the X-ray flux was measured for  $\eta$  Car, WR 22, and WR 25.  $\eta$  Car requires an additional time-variable thermal component in the spectral model, which is associated with the wind-wind collision zone.

**Conclusions.** Properties such as temperature, pressure, and luminosity of the X-ray emitting plasma in the Carina nebula derived from the eROSITA data are consistent with theoretical calculations of emission from superbubbles. This confirms that the X-ray emission is caused by the hot plasma inside the Carina nebula that has been shocked-heated by the stellar winds of the massive stars, in particular, of  $\eta$  Car.

**Key words.** stars: massive – ISM: bubbles – HII regions – ISM: structure – X-rays: ISM – X-rays: stars

## 1. Introduction

The Carina nebula complex (NGC 3372, hereafter CNC) is the brightest emission nebula in the southern Galactic plane at a distance of  $2.3 \pm 0.1$  kpc (Smith 2006; Shull et al. 2021; Göppel & Preibisch 2022). It harbours hundreds of protostars and several young stellar clusters (Trumpler 14, 15, and 16; Collinder 228 and 232; and Bochum 10 and 11) and is a giant H II region that was created by the radiation and winds from more than 60 OB stars, three Wolf-Rayet (WR) stars, and the massive binary  $\eta$  Carinae ( $\eta$  Car hereafter) in Trumpler 16 (Smith & Brooks 2008). In addition, at about  $1^\circ$  north-west of the CNC, an H II region around the stellar cluster NGC 3324, called the Gum 31 region, is located, with a similar distance as to the CNC (Kharchenko et al. 2005). Because of its proximity, the CNC is the ideal place for studying star formation and massive star feedback in the Milky Way.

Inside the CNC lie dark shells that are observed in the optical. Stars are being formed in these shells (Smith et al. 2000, 2010). Images taken with the *Hubble* and *Spitzer* Space Telescopes have revealed large pillars of dust in the nebula around  $\eta$

Car. A large amount of dust has also been found in observations in the sub-millimeter range (Preibisch et al. 2011b) and in the far-infrared (FIR, Preibisch et al. 2012). Observations of molecular line emission have revealed some dynamics in the dust shells with velocities that are different from those in the Carina arm, in which they are located (Whiteoak & Otrupcek 1984; Cox & Bronfman 1995; Brooks et al. 1998; Yonekura et al. 2005).

The CNC also contains molecular gas that may develop into new star-forming regions in the future (Smith & Brooks 2008). Three regions with different star formation properties have been detected in the CO data: Near  $\eta$  Car lie small globules, which are most likely surviving cores in the giant molecular cloud complex. Around Trumpler 14 lies the Northern Cloud, which shows little indication of star formation. In the south lies the Southern Cloud, which has been affected by the massive stars in Trumpler 16, and in which a second generation of stars is forming.

Active star formation is in particular observed in the dust pillars. In optical and infrared (IR) observations, more than 900 young stellar objects (YSOs) have been detected in the dust pillars (Smith et al. 2010) including protostars with ages of only  $10^5$  yr. The star formation in these dust pillars was most likely

triggered by winds from the massive stars. In the entire CNC, more than 60 000 young stars have been detected (Preibisch et al. 2011a). With this high rate of star formation, the CNC contributes significantly to the current star formation in the Milky Way (Povich et al. 2011; Preibisch et al. 2011a).

Soft X-ray emission has also been observed from the CNC with the *Einstein* Observatory (Seward & Chlebowski 1982) and ROSAT (Corcoran et al. 1995). Observations with *XMM-Newton* and *Suzaku* have shown a thermal spectrum with enhanced element abundances particularly of iron (Hamaguchi et al. 2007b; Ezoe et al. 2009). With the *Chandra* X-ray Observatory, diffuse X-ray emission was confirmed and analysed in a 1 Ms survey of the CNC (*Chandra* Carina Complex Project, CCCP, Townsley et al. 2011a,c). The spectral analysis of the diffuse emission has shown that the emission comes from thermal plasma, with indications of charge exchange, most likely between the hot plasma inside the nebula and the cold pillars, ridges, and clumps. The diffuse X-ray emission is most likely caused by the stellar winds of massive stars (Castor et al. 1975), but observations have also shown that the X-ray emitting plasma is not concentrated around the massive stars, but is distributed in broader areas. A bright hook is visible in X-rays that does not coincide with any prominent emission at longer wavelengths. In the east, the emission of the X-ray hook is aligned with the eastern arm of the striking V-shaped dust lane seen in the optical. The diffuse X-ray emission is brightest south of the western arm of the V-shaped dust lane. Some anti-correlation is seen between the diffuse X-ray emission and the 8  $\mu$ m IR emission, suggesting that the X-rays shine through holes in the distribution of heated dust. Alternatively, the bulk of the X-ray plasma is too hot and too tenuous to be seen, such that it only appears where that hot plasma pushes through the holes and mixes with gas from the rim of the hole. The mixing of the two reduces the temperature of the hot gas and increases its emission measure, and the gas appears in soft X-rays. This process is predicted from 3D hydrodynamic simulations to occur frequently whenever massive-star wind bubbles merge.

In this paper, we report studies of the diffuse emission of the CNC using the extended ROentgen survey with an Imaging Telescope Array (eROSITA; Merloni et al. 2012; Predehl et al. 2021) on board the Spektrum-Roentgen-Gamma (SpekTRG, SRG) spacecraft. eROSITA has performed all-sky surveys in the soft to medium X-ray energy band of 0.2–10 keV, which is particularly suited for the study of the hot phase of the interstellar medium (ISM). The all-sky surveys allow us to study the emission from the entire nebula with a uniform exposure and resolution. In addition, as emission in the surroundings is also observed, we are able to constrain the local X-ray background well. We present the study of the morphology and the spectra of the diffuse emission in different regions. We compare the physical parameters of the ISM derived from the eROSITA data with theoretical calculations. We have also analysed the emission of the X-ray brightest massive stars in the CNC and studied the time variability.

## 2. Data

### 2.1. eROSITA

The CNC was observed in the all-sky surveys of eROSITA on board the SRG, which was launched on July 13, 2019, from the Baikonur cosmodrome. There are seven telescope modules (TMs) on eROSITA, which are equipped with a CCD detector each. After the launch, it became obvious that two TMs have

light leaks (TM5 and 7) and therefore have a higher background. The effect is not yet well understood. Data taken with TM5 and 7 are therefore not included in the analysis presented here. eROSITA has a large field of view (FOV) with a diameter of  $\sim 1$  degree and high sensitivity in the energy range up to 10 keV, especially below 2.3 keV. It is thus the ideal telescope for studying the distribution and spectral properties of the large extended X-ray emission from the ISM. eROSITA is planned to perform a total of eight surveys of the entire sky (eROSITA all-sky survey, eRASS1-8; the total survey is called eRASS:8), out of which four surveys have been completed now (eRASS:4). We present the analysis of the eRASS:4 data of the CNC.

For the data processing and analysis, we have used the eROSITA Science Analysis Software System (eSASS, Brunner et al. 2022). We used the energy-calibrated event files from the eSASS pre-processing pipeline c020 and the eSASS user version 211214.

The CNC has an extent of about  $2^\circ \times 3^\circ$ . In order to fully cover the CNC and also to have data for estimating the local X-ray background, we used eRASS:4 data from a region with a size of  $\sim 10^\circ \times 5^\circ$  centred on the CNC.

### 2.2. HI

Archival data of HI  $4\pi$  (HI4PI) all-sky HI survey (HI4PI Collaboration 2016) were used in this work to compare the distribution of the hot interstellar plasma emitting X-rays with that of the cold diffuse gas. It is likely that the massive stars in the CNC have produced a cavity in the distribution of the cold atomic gas, which is filled with photo- and shock-ionised gas seen in the optical to X-rays. The HI4PI survey combines the Effelsberg-Bonn HI Survey (EBHI; Kerp et al. 2011; Winkel et al. 2016) and the Galactic All-Sky Survey (GASS; McClure-Griffiths et al. 2009; Kalberla et al. 2010; Kalberla & Haud 2015) obtained with the Parkes Telescope. The angular resolution is  $16''.2$ , corresponding to  $\sim 11$  pc at the distance of the Carina nebula (2.3 kpc; Smith 2006). The brightness temperature noise level is  $\sim 43$  mK at a velocity resolution of  $1.49$  km s $^{-1}$ .

## 3. Diffuse emission

### 3.1. Images

Using the energy-calibrated data of eRASS:4, we created images in the energy bands of 0.2–10.0 keV, 0.2–0.5 keV, 0.5–1.0 keV, 1.0–2.0 keV, and 2.0–10.0 keV. The data were stored in partly overlapping sky tiles with a size of  $3.6^\circ \times 3.6^\circ$  each. First, we merged the event files of the sky tiles and recalculated the sky coordinates with the CNC in the centre (RA = 10:43:72.8, Dec =  $-59:49:48$ ). Images were created for each energy band using a bin size of 400, that is, one image pixel has a size of  $20'' \times 20''$ . Based on the images, vignetting-corrected exposure maps and exposure-corrected count-rate images were created. The average exposure time was  $\sim 620$  s. In addition, we created event files and images without point sources (called ‘point-source-free’ data hereafter). We excluded all significantly detected point sources from the data. We used the standard eRASS point source catalogue of eRASS:4 produced by the consortium with a circular extraction region with a radius of three times the half-energy width (HEW) of  $14.5''$  (Merloni et al. 2024, for the catalogue of the first all-sky survey eRASS1). In the  $\sim 10$  deg $^2$  field around the CNC, we excluded  $\sim 3000$  sources. For  $\eta$  Car, which is the brightest X-ray source in the CNC, we used a circular extraction region with a radius of  $64''$ , that is, three times larger than the HEW

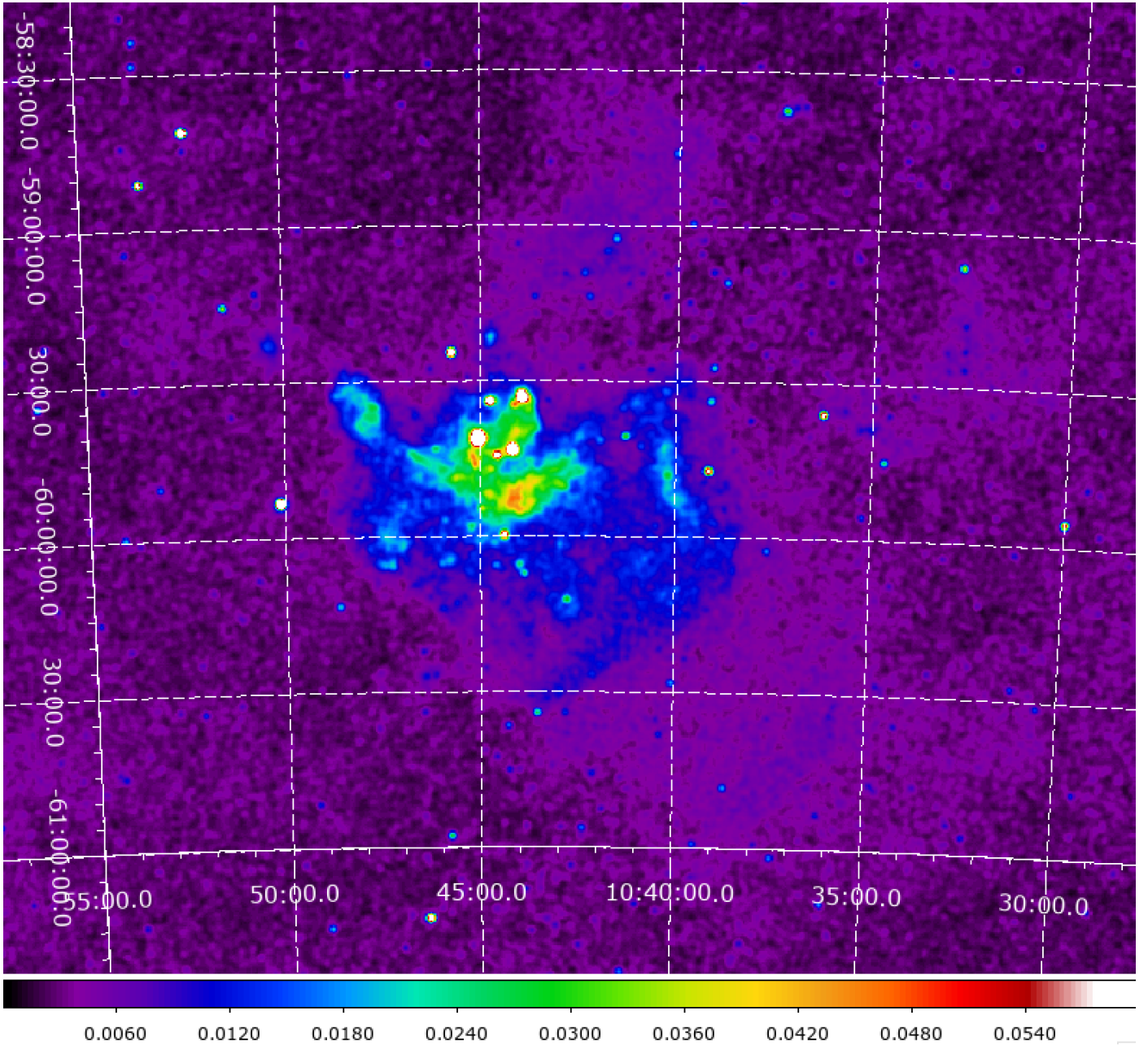


**Fig. 1.** Exposure-corrected eROSITA broad-band image (0.2–10.0 keV, 0–0.06 cts s<sup>-1</sup>) in equatorial coordinates. The image is shown using a linear intensity scale.

of eROSITA at higher energies (29'' below 3 keV and 42'' at 4.5 keV, Dennerl et al. 2020), to remove as much emission from this source as possible. Using these filtered data, we binned the images again with a bin size of 400 and created exposure maps and count-rate images in the same energy bands as for the complete data. The count-rate image in the full band (0.2–10.0 keV) is shown in Fig. 1, and a three-colour image of the point-source-free data in the bands 0.2–0.5 keV, 0.5–1.0 keV, and 1.0–2.0 keV is shown in Fig. 2a with the regions we extracted for the spectral analysis (Sect. 3.2).

The eROSITA images show significant diffuse emission in the Central region, where the open clusters Trumpler 14, 16, and Collinder 232 as well as  $\eta$  Car and the Wolf–Rayet star WR25 are located. Around the massive stars, there is significant emission above 1 keV (appearing blue in the three-colour image

in Fig. 2a in the Central region 1 (C1) around Trumpler14), indicating emission from the stellar winds. The emission at the position of the stellar cluster Trumpler 15 is also bright above 1 keV.

There is bright and soft extended X-ray emission south of Trumpler 14, which extends to the east, beyond Trumpler 16 and Collinder 232 (Central region 2, C2). The Carina nebula is very bright in this region in the optical (see Fig. 2b) and in the radio continuum (Rebolledo et al. 2021, see Sect. 5.1). The gas seems to be strongly photoionised from the radiation of the massive stars of the stellar clusters,  $\eta$  Car and WR25.

The most pronounced structure in X-rays is the X-ray hook. It appears green in the three-colour image, indicating that the emission is dominated around 1 keV, with more contribution of emission above 1 keV than in the adjacent C2 region.



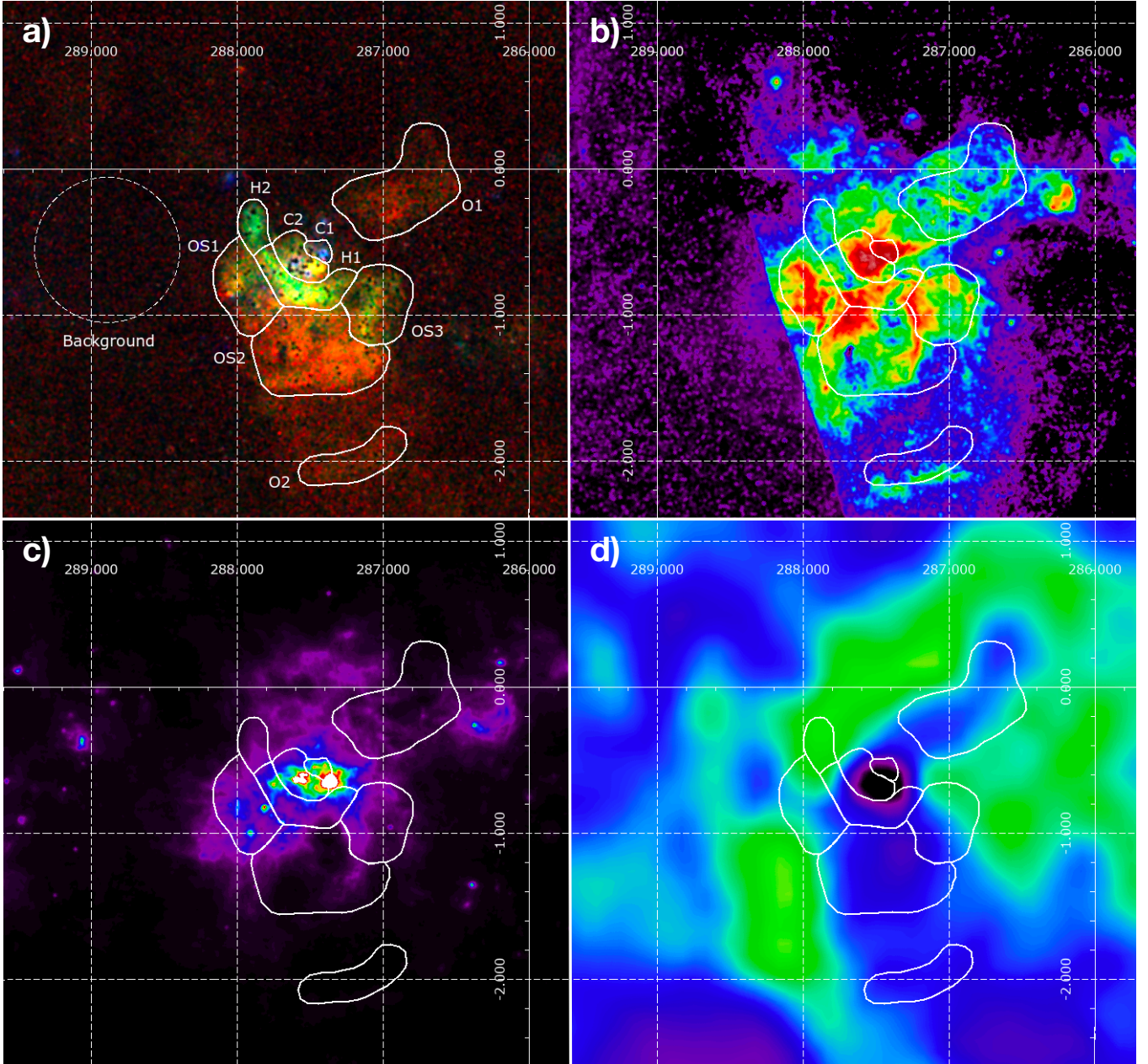


**Fig. 2.** a) Exposure-corrected eROSITA three-colour image using point-source-free images of the three softer bands (red for 0.2–0.5 keV, green for 0.5–1.0 keV, and blue for 1.0–2.0 keV). b) Optical *R*-band image showing the mainly photoionised gas (2nd Digitized Sky Survey, *R* image, 6000–26 000 [arbitrary units]). c) IR image of cold dust with AKARI in the 60  $\mu\text{m}$  band (Doi et al. 2015, 0–15 000 MJy sr<sup>-1</sup>). d) HI map of HI4PI survey (HI4PI Collaboration 2016, 0–1500), with the extraction regions for the spectral analysis shown in white. The labels are C1 for Central region 1, C2 for Central region 2, H1 for Hook region 1, H2 for Hook region 2, OS1 for Outskirt region 1, OS2 for Outskirt region 2, OS3 for Outskirt region 3, O1 for Outer region 1, and O2 for Outer region 2. The dashed circle shows the region from which the spectrum of the local background was extracted. All images are shown in Galactic coordinates using a linear intensity scale.

Next to the X-ray hook (Hook regions 1 and 2, H1 and H2, respectively), there is emission mainly between 0.5 keV and 1.0 keV, indicating hot thermal plasma (Outskirt regions 1 and 3, OS1 and OS3). In these region, shell-like structures are seen in the photoionised gas (Fig. 2b) that are also traced by dust (Fig. 2c).

Towards lower Galactic latitudes, the emission is soft (around 0.5 keV) and rather faint and diffuse (Outskirt region 2, OS2, and farther out; it is a little brighter in the Outer region 2, O2). Similar emission is also observed to the north (Outer region

1, O1). The HI map (Fig. 2d) shows soft faint emission that seems to indicate hot gas escaping into cavities in the cold gas distribution.

### 3.2. Spectra

For the spectral analysis, we used the point-source-free data. Therefore, the emission from the massive stars in  $\eta$  Car, for example, is not included in the diffuse emission, but is addressed separately (see Sect. 4). For the analysis of the diffuse emission,

however, we have to take into account that there might be contamination by the emission of the very bright X-ray sources in the areas around them.

We first defined extraction regions based on the photon statistics using the Voronoi tessellation algorithm (Cappellari & Copin 2003). However, the diffuse emission from the CNC is very faint. Even for a signal-to-noise ratio as low as 40, no reasonable spectra were obtained, which would have allowed the analysis of the emission of the Carina nebula above the background.

Therefore, we decided to define the extraction regions manually in the next step, based on the comparison to multi-wavelength data (see Fig. 2 and Sect. 3.1). The criteria we applied are the following:

- contiguous emission in X-rays with sufficient photon statistics,
- similar colour in the three-colour X-ray image, indicating a similar spectrum,
- corresponding to known astrophysical objects or structures (stellar clusters, molecular clouds, or interstellar cavities),
- well correlated with distribution observed at other wavelengths (photoionised gas seen in the optical or radio, dust, molecular clouds, and atomic gas).

The extraction regions are shown in Fig. 2. The region from which the spectrum was extracted to estimate the local X-ray background is shown with a dashed circle in the upper left panel.

We analysed the spectra using XSPEC version 12.12.1. All spectra are contaminated with particle-induced non-X-ray background as well as with local astrophysical X-ray background (see Freyberg et al. 2020; Yeung et al. 2023). An additional spectrum was extracted in a region near but well outside the CNC to estimate the local X-ray background. The background was first modelled and fit, and then, the source spectrum (for regions in the CNC) was simultaneously fit with the background spectrum, also including the background components. The particle background can be described with a multi-component power-law spectrum with emission lines arising in the instruments. In order to estimate the particle background, we used the data up to 9.0 keV, even though no diffuse emission was observed above  $\sim 3.0$  keV in most cases (above  $\sim 5.0$  keV in the C1 region). The astrophysical X-ray background consists of emission from the Local Hot Bubble, the Galactic disc and halo, and the extragalactic X-ray background. The spectral model parameter values that were obtained from the fit of the spectrum of the background region, were also used for the fit of the source spectrum, from which the background was not subtracted. The background model components were scaled with a multiplicative constant parameter that mainly accounts for the different size of the extraction regions, but was free in the fit. For example, the area of Central regions C1 and C2 is  $0.019 \text{ deg}^2$  and  $0.076 \text{ deg}^2$ , while the area of the local background region is  $0.785 \text{ deg}^2$ . The theoretical scaling factor therefore is 0.024 and 0.096 for regions C1 and C2, respectively. The best fit yielded a scaling factor of 0.02 ( $< 0.046$ ) for C1 and 0.11 (0.06–0.23) for C2, with the 90% confidence limits given in brackets.

X-ray observations of the ISM in the Milky Way and nearby galaxies have shown that the emission is well reproduced with at least two thermal plasma components with different temperatures (e.g. Kuntz & Snowden 2010; Kavanagh et al. 2020, and references therein). The component with the lower temperature has  $\sim 0.2$  keV and indicates emission from the hot phase of the ISM in equilibrium. The component with the higher temperature has temperatures  $> 0.5$  keV and is particularly significant in regions with recent additional heating (H II regions,

superbubbles, and supernova remnants, SNRs). To model the plasma emission, we used the collisional ionisation equilibrium (CIE) model `vpec1` and the non-equilibrium ionisation model `vnei` (Borkowski et al. 2001, and references therein).

We also fitted the element abundances, in particular, for O and Fe. In all regions, the fits of the eROSITA spectra suggest that the element abundances are consistent with solar values. At first glance, this appears to contradict the results of Townsley et al. (2011a), who found enhanced abundances of O, Ne, and Mg in a few smaller regions and super-solar abundances of Si, S, and Fe in the CNC. However, because eRASS is a shallow survey, as our first tessellation approach has shown, the photon statistics are not sufficient to analyse small regions. Therefore, enhancements of O, Ne, or Mg seen in small regions in the deep *Chandra* data will be dominated by the emission from plasma with solar abundances in larger regions. Moreover, there is an Al-K instrumental line at 1.5 keV in the eROSITA data, and the sensitivity drops significantly above 2 keV, which makes it impossible to constrain the abundances of Si, S, and Fe.

In Central regions C1 and C2, and to some extent, also in Hook regions H1 and H2, the emission appears to be harder than in the other regions. Townsley et al. (2011a) have shown that this emission is well reproduced by one or two additional thermal components with higher temperatures, accounting for possible emission from pre-main-sequence stars or  $\eta$  Car, for example. We therefore fit the spectra in these regions with additional thermal components. An alternative scenario for the hard emission is that particles are accelerated in shocks of stellar winds and can give rise to a non-thermal component in the X-ray regime as well. To verify the existence of such a component, we also included a power-law emission component (`powerlaw`) in some regions. Townsley et al. (2011a) also considered a non-thermal component in the diffuse emission of the Carina nebula, but neither presented nor discussed any spectral fit results including a power-law component.

To account for absorption, we used the model `tbvarabs` (Wilms et al. 2000). The spectra of the local background and the source regions with the best-fit models are shown in Fig. 3, and the spectral fit parameters are listed in Table 1.

Extraction region C1 covers the emission around Trumpler 14 and Collinder 232, which are seen as bright point-like sources and were removed. The diffuse emission is hard, and the spectrum shows significant emission above 1 keV without emission line features. For the source spectrum, an additional emission component is necessary to reproduce the emission between 1 and 5 keV. We first added a third thermal plasma component for the source model. As an alternative, we also fit the spectrum including a power-law component instead of the third thermal component. The model with a third thermal component and the model with a non-thermal component yield similarly good fits. A model including two additional thermal components with  $kT = 2.5, 6.0$  keV similar to the model of Townsley et al. (2011a) for the hard emission also yields comparable fit statistics. When we assume one additional thermal component, the temperature becomes very high ( $kT = 6.8$  (4.7–12) keV; the 90% confidence range is given in brackets), which is rather unphysical for shocked interstellar plasma. The spectrum is fit well with a combination of a two-component thermal plasma model assuming non-equilibrium ionisation (NEI) with  $kT = 0.24$  keV and 0.82 keV and a power-law component with photon index  $\Gamma = 1.7$  (1.3–2.2), which can be explained by a population of non-thermal electrons. A cavity is seen in the HI map (Fig. 2d).

<sup>1</sup> <http://atomdb.org/>

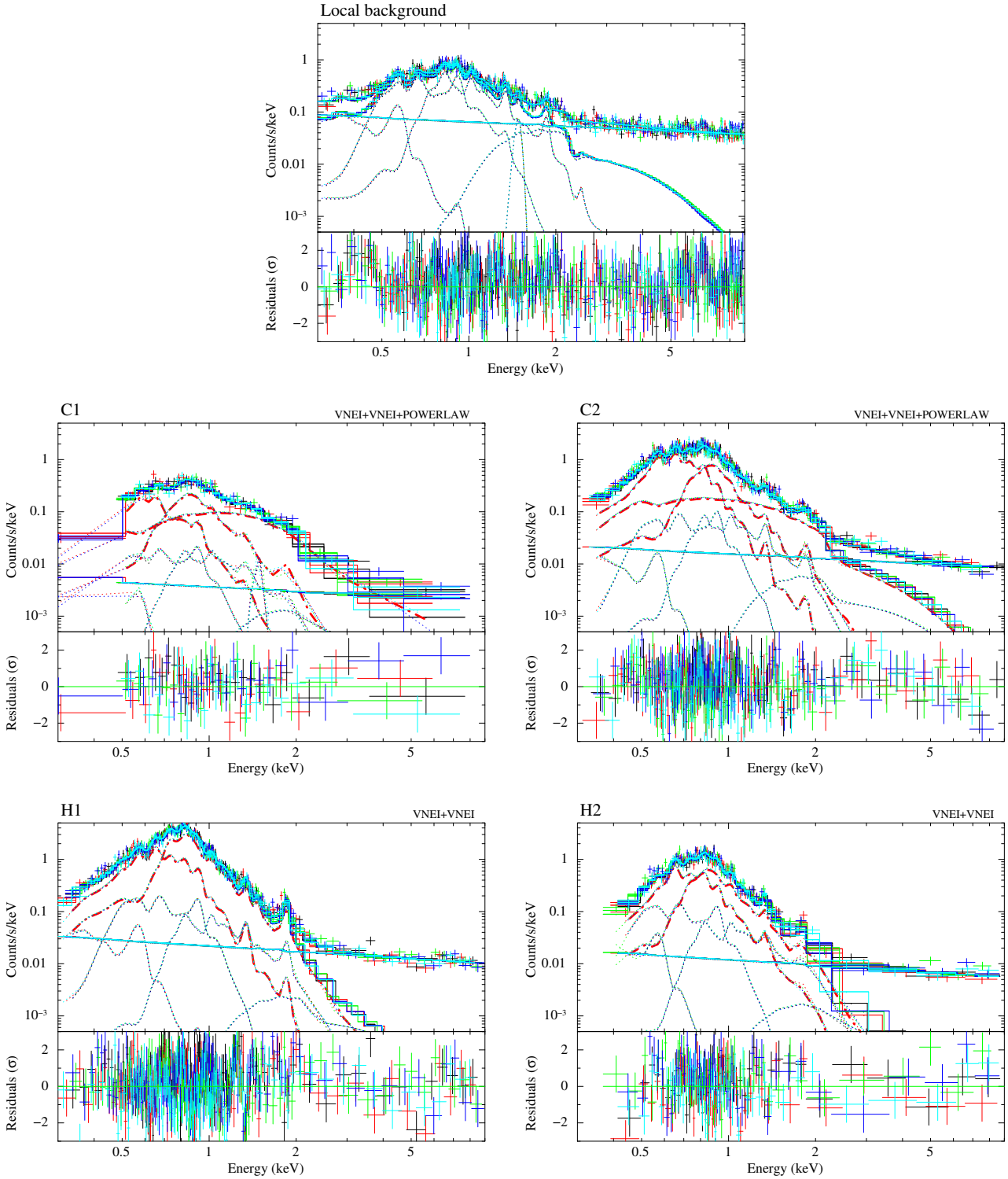


**Fig. 3.** eROSITA TM1–4,6 spectra shown in black, red, green, blue, and cyan. For each TM, we show the spectral model components with the corresponding colours (the cyan lines are visible best) with dotted lines. The model also includes the particle background (seen as a straight line) and local X-ray background components. In addition, we mark the source components with thick dash-dotted red lines. The extraction regions are indicated in the upper left corner of each panel.

Most likely, the cold material around the stellar clusters has been ionised and blown away by the radiation and the stellar winds of the massive stars in the clusters.

Region C2 shows diffuse emission around Trumpler 16. The bright X-ray emission from the massive star binary  $\eta$  Car and from the star WR25 along with other detected point sources

inside the region was removed. The emission appears yellowish in the three-colour-image (Fig. 2a), with dominant emission in the medium band, but also significant contributions from the soft and hard bands. The best-fit model requires two thermal NEI plasma components ( $kT = 0.28$  keV and  $0.82$  keV with  $n_e t \approx 10^{11}$  cm $^{-3}$  s for both) and an additional harder component.



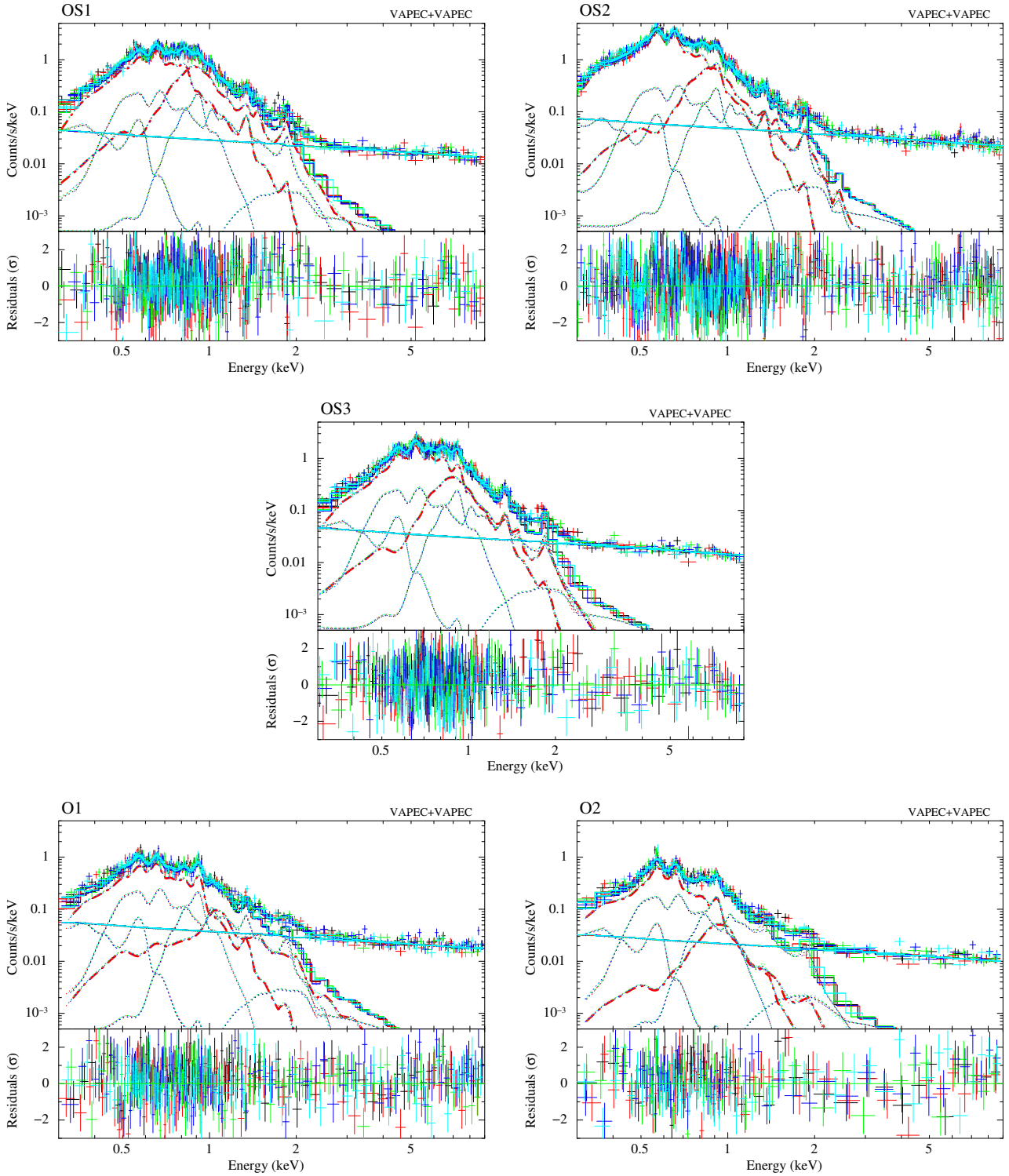


Fig. 3. continued.

In this region, the fit with a non-thermal component is preferred to a fit with two additional thermal components as in [Townesley et al. \(2011a\)](#) with  $\chi^2 = 513$  and degrees of freedom (dof) = 468 compared to  $\chi^2 = 561$  and dof = 466 for a purely thermal model. When we again assume one additional thermal component, the fit yields a very high temperature of  $kT = 15$  keV with a lower limit of 9 keV (unconstrained to higher values). In the best-fit model, the non-thermal component has a photon index of

$\Gamma = 1.8$  (1.5–2.3). This component again suggests the existence of non-thermal electrons.

Next to region C2, we defined the X-ray Hook region H1, which is located south of the triangular bright region in the optical and IR, which in part also coincides with our region C2 (Figs. 2b and c). Relative to the massive star clusters in the CNC, the X-ray hook is located outside the bright photoionised nebula, which is indicative of a shock of the expanding H II region.

**Table 1.** Spectral fit parameters.

		Central regions		Hook regions	
Region	C1	C2	H1	H2	
model	2vnei+powerlaw	2vnei+powerlaw	2vnei	2vnei	
$N_{\text{H}}$ ( $10^{22}$ cm $^{-2}$ )	0.28 (0.21–0.35)	0.13 (0.10–0.17)	0.13 (0.11–0.17)	0.25 (0.20–0.30)	
$kT_1$ (keV)	0.24 (0.15–0.25)	0.28 (0.23–0.39)	0.26 (0.23–0.29)	0.27 (0.25–0.32)	
$\tau_1$ (cm $^{-3}$ s)	2.4e+11 (>1.7e+10)	1.8e+11 (6.2e+10–3.9e+11)	2.7e+11 (1.7e+11–5.4e+11)	6.5e+11 (2.5e+11–1.3e+12)	
norm $_1$	1.8e–3 (3.7e–4–2.5e–2)	3.7e–3 (2.0e–3–7.6e–3)	1.3e–2 (0.8e–2–2.3e–2)	6.2e–3 (3.2e–3–9.9e–3)	
$kT_2$ (keV)	0.82 (0.76–0.86)	0.82 (0.76–0.86)	0.63 (0.62–0.65)	0.70 (0.67–0.77)	
$\tau_2$ (cm $^{-3}$ s)	1.9e+11 (>1.3e+11)	3.0e+11 (>1.3e+11)	3.0e+13 (>1.6e+12)	3.3e+11 (2.3e+11–4.9e+11)	
norm $_2$	6.4e–4 (3.6e–4–2.0e–3)	1.3e–3 (1.0e–3–2.1e–3)	1.3e–2 (1.1e–3–1.4e–3)	2.6e–3 (1.9e–3–3.2e–3)	
norm $_2$ /norm $_1$	0.35	0.35	1.0	0.42	
$\Gamma$	1.7 (1.3–2.2)	1.8 (1.5–2.3)			
norm $_p$	1.3e–3 (1.0e–3–1.8e–3)	2.3e–3 (1.7e–3–3.0e–3)			
$\chi^2$	111.36	513.73	872.00	323.29	
DOF	126	468	661	256	
$F_{\text{abs}}^{(\dagger)}$ (erg s $^{-1}$ cm $^{-2}$ )	8.7e–12	2.2e–11	3.4e–11	7.6e–12	
$F_{\text{unabs}}^{(\dagger)}$ (erg s $^{-1}$ cm $^{-2}$ )	1.9e–11	4.0e–11	7.5e–11	2.8e–11	
$A^{(*)}$ (deg $^2$ )	0.019	0.076	0.140	0.061	
Outskirts					
Region	OS1	OS2	OS3		
model	2vapec	2vapec	2vapec		
$N_{\text{H}}$ ( $10^{22}$ cm $^{-2}$ )	0.21 (0.19–0.24)	0.15 (0.13–0.16)	0.19 (0.17–0.22)		
$kT_1$ (keV)	0.21 (0.20–0.22)	0.19 (0.18–0.20)	0.22 (0.21–0.23)		
norm $_1$	4.8e–2 (3.9e–2–6.0e–2)	1.0e–1 (9.5e–2–1.2e–1)	2.9e–2 (2.3e–2–3.7e–2)		
$kT_2$ (keV)	0.83 (0.80–0.86)	0.80 (0.76–0.84)	0.80 (0.76–0.86)		
norm $_2$	6.1e–3 (5.2e–3–7.0e–3)	5.7e–3 (4.7e–3–6.6e–3)	2.1e–3 (1.8e–3–2.5e–3)		
norm $_2$ /norm $_1$	0.13	0.057	0.072		
$\chi^2$	735.26	1151.54	586.15		
DOF	601	898	569		
$F_{\text{abs}}^{(\dagger)}$ (erg s $^{-1}$ cm $^{-2}$ )	1.8e–11	4.1e–11	1.6e–11		
$F_{\text{unabs}}^{(\dagger)}$ (erg s $^{-1}$ cm $^{-2}$ )	9.5e–11	1.9e–10	7.0e–11		
$A^{(*)}$ (deg $^2$ )	0.187	0.429	0.195		
Outer regions					
Region	O1	O2			
model	2vapec	2vapec			
$N_{\text{H}}$ ( $10^{22}$ cm $^{-2}$ )	0.18 (0.16–0.20)	0.12 (0.09–0.15)			
$kT_1$ (keV)	0.20 (0.19–0.21)	0.19 (0.18–0.20)			
norm $_1$	3.2e–2 (2.6e–2–3.9e–2)	9.3e–3 (6.9e–3–1.3e–2)			
$kT_2$ (keV)	1.7 (1.4–2.0)	0.98 (0.80–1.20)			
norm $_2$	2.7e–3 (2.1e–3–3.3e–3)	2.5e–4 (1.6e–4–3.4e–4)			
norm $_2$ /norm $_1$	0.084	0.027			
$\chi^2$	535.60	329.11			
DOF	511	287			
$F_{\text{abs}}^{(\dagger)}$ (erg s $^{-1}$ cm $^{-2}$ )	1.1e–11	4.6e–12			
$F_{\text{unabs}}^{(\dagger)}$ (erg s $^{-1}$ cm $^{-2}$ )	5.7e–11	1.9e–11			
$A^{(*)}$ (deg $^2$ )	0.343	0.150			

**Notes.** The 90% confidence interval is given in brackets.  $^{(\dagger)}$ Absorbed and unabsorbed flux in the energy band of 0.2–10.0 keV.  $^{(*)}$ Size of the extraction region.



The emission appears yellow-green, with dominant emission between 0.5–1.0 keV. The spectrum is well reproduced with two thermal components with  $kT = 0.26$  keV and 0.63 keV, with the first being consistent with NEI ( $n_e t = 2.7 \times 10^{11} \text{ cm}^{-3} \text{ s}$ ), while the hotter component seems to have reached collisional ionisation equilibrium (CIE). In this region, the contribution of the hotter component is as strong as that of the cooler component ( $\text{norm}_2/\text{norm}_1 = 1$ ), while in the other regions, it is less than half ( $\text{norm}_2/\text{norm}_1 < 0.42$ ) or almost negligible. Both the high ionisation timescale and the relatively high brightness (and hence high  $\text{norm}_2$ ) for the hotter component suggest that the gas might be highly compressed.

The tip of the X-ray hook (region H2) appears greener than region H1. While region H1 traces the edge of a cavity seen in HI (Fig. 2d), region H2 coincides with a larger HI structure seen in the north. The spectrum of region H2 suggests a similar intrinsic spectrum as in region H1 (two thermal components with two temperatures), while the hotter component also seems to be in NEI in the region H2. The foreground absorption is higher in this region ( $N_{\text{H}} = 2.5 (2.0\text{--}3.0) \times 10^{21} \text{ cm}^{-2}$ ), suggesting that the tip of the X-ray hook is located inside or behind the HI structure. Neither Hook region contains indications of a non-thermal component.

The other regions, in which there is diffuse X-ray emission with a sufficient surface brightness that allows us to perform a spectral analysis reasonably well, the emission appears red to orange, with most of the emission below 1 keV (regions OS1, OS2, OS3 as well as O1 and O2). These regions coincide with lower-density regions in the HI map. Most likely, this is emission from hot plasma that escapes from the central active regions. The spectra are well reproduced with two thermal components for plasma in CIE with a lower-temperature component with  $kT \approx 0.2$  keV and a higher-temperature component with  $kT > 0.8$  keV. Region O2 extends north of and along a broad optical filament and likely is photoionised gas delineating the end of the cavity. The hot gas streaming through the HI cavity will likely be adiabatically compressed (hence heated) because it is being pushed against the HI cavity wall. Mixing with HI gas then creates the more luminous, colder component. The fact that the region O2 is spatially anti-correlated with the optical region to the south suggests that the cavity is elongated southwards approximately in the plane of the sky. Region O1 is also associated with optical emission, but in this case, X-rays and optical emission are more co-spatial, which suggests that the associated HI cavity is significantly inclined to the plane of the sky.

#### 4. Stellar sources

The CNC contains several X-ray bright point sources associated with massive stars and stellar systems that have been studied extensively over the last decades (see e.g. the *Chandra* based CCCP; Townsley et al. 2011c; Gagné et al. 2011; Nazé et al. 2011). While the CNC harbours thousands of young stars, only the X-ray brightest ones are detected as individual sources in eRASS (see Table A.1). In our analysis of the eRASS data, we therefore focus on the prominent X-ray sources in the region, that is, on  $\eta$  Car itself, on several O-type stars and binaries, and on the Wolf–Rayet stars WR 22, WR 24, and WR 25. An intensity-scaled eRASS image with the studied stars and the source regions we used is shown in Fig. 4.

For the point source analysis, events from all TMs were used. Source and background photons were extracted from adapted

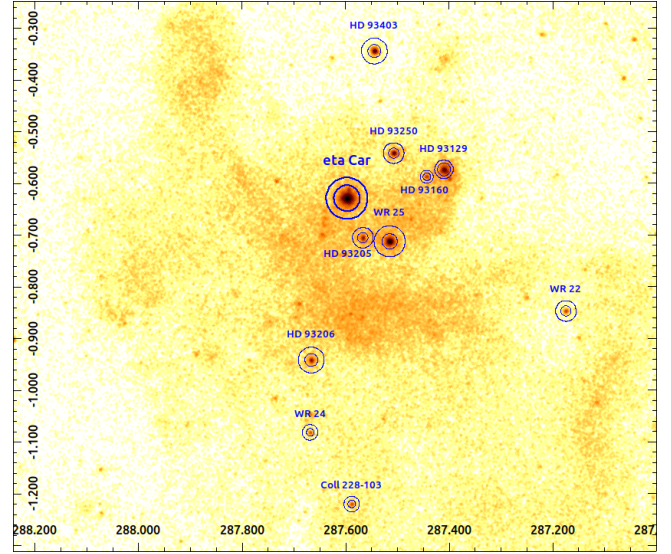


Fig. 4. eRASS:4 image and stellar sources with extraction regions in Galactic coordinates.

circular and annular regions, respectively. While some minor contributions from other nearby stars and diffuse emission are present, the photon distribution for the eRASS sources discussed here in most cases is strongly dominated by the X-ray emission from a single star or a stellar system. With the exception of  $\eta$  Car, we used the eRASS:4 combined spectra in our analysis and thus derived the average properties of the sources. The X-ray spectra were fit with absorbed multi-temperature CIE plasma models (apec) with errors denoting the 90% confidence range. A foreground column density of  $2 \times 10^{21} \text{ cm}^{-2}$  was used to account for the interstellar foreground absorption, and the adopted distance to the CNC was 2.3 kpc.

During the eRASS mapping, the region was observed four times with a long-term sampling of about 0.5 yr. The exposure times per individual eRASS, obtained in multiple scans over two to three days, are about 0.5 ks and provide sufficient photons to study the X-ray variability for our targets. Example light curves of three selected X-ray sources are shown in Fig. 5.

##### 4.1. $\eta$ Carinae

$\eta$  Carinae (HD 93308), the most prominent stellar object in the CNC, is a very massive stellar binary in a highly eccentric 5.5 yr orbit located in Trumpler 16. It consists of an eruptive primary in its luminous blue variable (LBV) phase and a secondary, potentially evolved high-mass star with mass estimates of  $M_1 \gtrsim 80\text{--}10$  and  $M_2 \gtrsim 30\text{--}40 M_{\odot}$ . A discussion of the  $\eta$  Car binary parameters can be found, for example, in Corcoran et al. (2001); Kashi & Soker (2016). In this system, the collision of the fast wind from the secondary and the slower but more massive wind from  $\eta$  Car A leads to the complex and variable X-ray emission and absorption scenarios over the orbit, especially around periastron (see, e.g., Pittard & Corcoran 2002; Hamaguchi et al. 2007a; Corcoran et al. 2017).

X-rays from  $\eta$  Car include emission from the outer structures created by the ejecta of the last eruptions, such as the famous Homunculus nebula and a more absorbed and variable hard component from the shock regions of the inner wind (Corcoran et al. 2022). The source is not spatially resolved by eROSITA, and

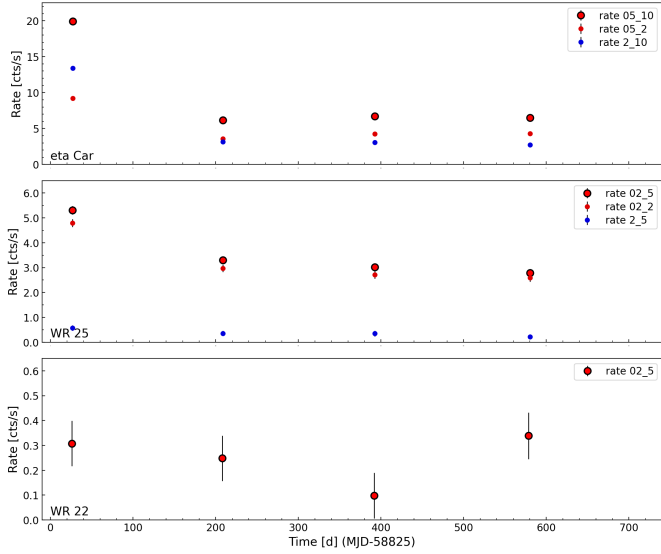


**Fig. 5.** Light curves of stellar sources in the CNC from eRASS, here highlighting the X-ray brighter targets  $\eta$  Car, WR 25, and WR 22, and their variability. The legend denotes the energy band in keV of the respective light curve (e.g. 05\_10: 0.5–10 keV).

the data provide a combined source spectrum. Because the star is bright in the optical and IR ( $G = 4.0$  mag,  $J = 1.7$  mag), a mild contamination from optical loading is present at energies of  $\lesssim 0.3$  keV that was included as a background component in the modelling. The combined eRASS data were first used to derive a baseline model that describes the non-variable spectral components in our  $\eta$  Car data. We then studied the variability between the individual eRASS visits. Particularly in eRASS1, the data taken on January 2–5, 2020, stand out because this observation covers the X-ray bright state before the periastron passage. The obtained spectra are shown in Fig. 6.

The X-ray emission from the stable component that is associated with the outer ejecta and nebula around  $\eta$  Car is well described by a two-temperature plasma with components at  $kT_{1,2} = 0.15$  keV and 0.7 keV, with the ratio of the emission measures  $EM_1/EM_2 \approx 1$ , a high N overabundance by a factor of 15, and an absorption column fixed at the ISM value of  $N_H = 2 \times 10^{21} \text{ cm}^{-2}$ . From the observed  $F_X = 1.8 \times 10^{-12} \text{ erg cm}^{-2} \text{ s}^{-1}$ , we derive an emitted 0.2–10.0 keV X-ray luminosity of  $3.7 \times 10^{33} \text{ erg s}^{-1}$  for the emission from the surrounding region. The outer ejecta is well described by a constant emission component in our data, but a slow temporal evolution is expected for the expanding nebula. Comparing our eRASS results with older X-ray measurements, we find that the derived flux from the combined eRASS 2020 and 2021 data matches the long-term trend seen in X-rays, which indicates a  $t^{-3}$  flux decline, as deduced from a fit to *XMM-Newton* EPIC-pn data from observations performed between 2003 and 2015 (Corcoran et al. 2022). For the 0.3–1.0 keV energy band, we obtained  $F_X = 1.3 \pm 0.1 \times 10^{-12} \text{ erg cm}^{-2} \text{ s}^{-1}$  from our spectral model, which matches the fitted X-ray trend over two decades well and supports the scenario for the Great eruption and the blast wave evolution.

Furthermore, a stronger absorbed and variable plasma component is detected. It is thought to be associated with the wind-wind collision zone, and one or two hot plasma components are required to model the eRASS spectra. Being most

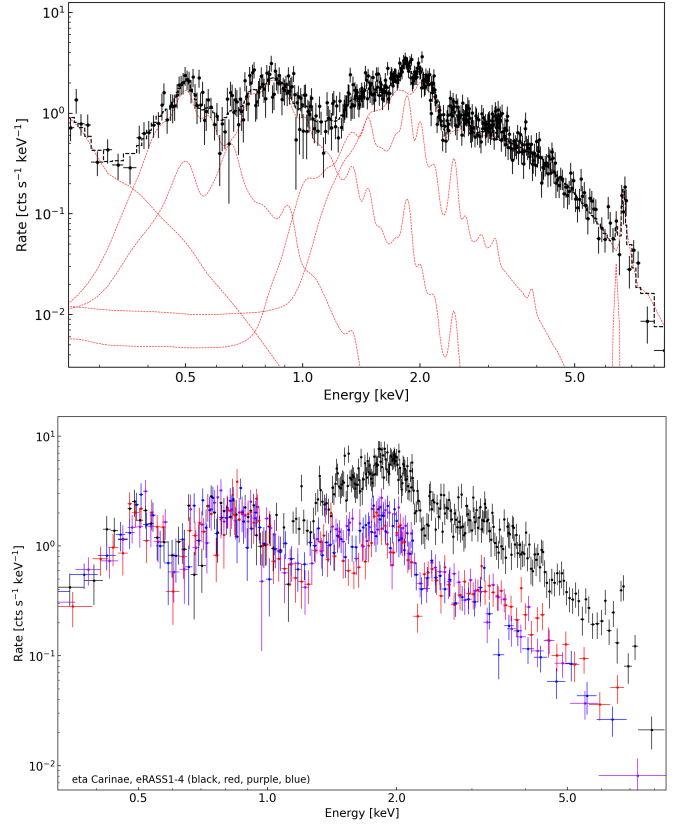


**Fig. 6.** Spectra of  $\eta$  Car as observed with eROSITA. Top: combined eRASS:4 spectrum with the spectral model (black) and the model components (red). Bottom: eRASS 1-4 spectra, shown in black, red, purple, and blue.

prominent during the bright state, Fe  $K\alpha$  6.4 keV emission is detected, for instance with a line flux of  $4.7 \times 10^{-4} \text{ photons s}^{-1}$  in eRASS1. To place our data into context, we used the orbital X-ray phasing,  $\text{MJD}_{\text{min}} = 50799.4 + 2023.4 \times n$ , following Corcoran et al. (2017).

In total, the mean eRASS X-ray luminosity of  $\eta$  Car in the 0.2–5.0 + 5.0–10.0 keV band is  $(2.8 + 2.9) \times 10^{34} \text{ erg s}^{-1}$  (observed),  $(3.1 + 2.9) \times 10^{34} \text{ erg s}^{-1}$  (ISM  $N_H$  corrected) and  $(13.0 + 3.1) \times 10^{34} \text{ erg s}^{-1}$  (fully corrected for  $N_H$ ). The eRASS1-4 spectral modelling results for  $\eta$  Car are summarised in Table 2.

The object  $\eta$  Carinae has been monitored in X-rays over several decades. The flux variability and spectral changes observed during the eRASS are similar to those observed over previous orbits (Corcoran et al. 2017) and agree overall with findings from NICER observations around the 2020 periastron passage (Espinoza-Galeas et al. 2022). However, the fluxes given by eRASS data are about 30% lower in the 2.0–10.0 keV band when compared to the NICER values. Although the data were not taken strictly simultaneously, this indicates cross-calibration issues that might be caused by effective area uncertainties at energies above  $\approx 2$  keV for the eROSITA survey data. A comparison of the derived fluxes from the two instruments is shown in Fig. 7. Based on the errors, the eRASS data are well described by a two-temperature model with  $kT_1 = 0.8$ –1.0 keV and  $kT_2 = 4.0$ –4.5 keV. Notably, the eRASS2 data at phase 0.068 are better described by a temperature of roughly 3 keV, and similarly, the NICER spectral models give 3.0–3.6 keV for data taken within a few days. However, it is also during a phase of quite strong

**Table 2.** Spectral model for the inner wind-wind collision zone emission in  $\eta$  Car.

Phase	$F_X^{\text{obs}}$ $10^{-11} \text{ erg cm}^{-2} \text{ s}^{-1}$	$N_{\text{H}1}$ $10^{22} \text{ cm}^{-2}$	$kT_1$ keV	$\text{EM}_1$ $10^{57} \text{ cm}^{-3}$	$N_{\text{H}2}$ $10^{22} \text{ cm}^{-2}$	$kT_2$ keV	$\text{EM}_2$ $10^{57} \text{ cm}^{-3}$	$\chi_{\text{red}}^2$ (dof)
0.979	20.8, 19.8	$3.10^{+1.26}_{-0.54}$	$0.54^{+0.33}_{-0.28}$	$0.49^{+9.94}_{-0.29}$	$3.79^{+0.35}_{-0.31}$	$5.36^{+1.23}_{-0.87}$	$1.50^{+0.17}_{-0.14}$	1.04 (264)
0.069	4.9, 4.5	$3.28^{+0.53}_{-0.51}$	$0.99^{+0.17}_{-0.17}$	$0.24^{+0.11}_{-0.09}$	$9.84^{+4.61}_{-2.71}$	$2.75^{+1.76}_{-0.86}$	$0.85^{+0.89}_{-0.35}$	0.95 (109)
0.160	3.9, 3.4	3.5	$0.53^{+0.67}_{-0.22}$	$0.25^{+0.59}_{-0.15}$	3.5	$3.63^{+4.01}_{-0.68}$	$0.34^{+0.05}_{-0.13}$	1.02 (98)
0.253	3.6, 3.1	3.1	$0.96^{+0.55}_{-0.59}$	$0.12^{+0.08}_{-0.06}$	3.1	$4.32^{+9.57}_{-1.38}$	$0.25^{+0.08}_{-0.10}$	0.92 (98)

**Notes.** The observed  $F_X$  is the total source flux in the 0.2–10.0 keV and 2–10 keV bands. The  $\eta$  Car spectrum includes emission from the surrounding nebula, described by a 2-T vapec model:  $N_{\text{H}} = 2 \times 10^{21} \text{ cm}^{-2}$ ,  $kT_1 = 0.15 \text{ keV}$ ,  $kT_2 = 0.7 \text{ keV}$ ,  $\log \text{EM}_1 = 55.80 \text{ (cm}^{-3}\text{)}$ ,  $\log \text{EM}_2 = 55.76 \text{ (cm}^{-3}\text{)}$ , and  $N = 15 \times \text{solar}$ , and solar abundances otherwise. For eRASS 3+4, a single  $N_{\text{H}}$  was used.

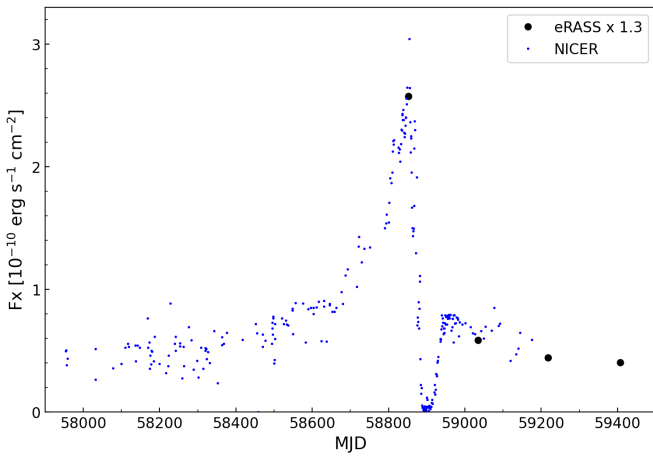


**Fig. 7.** X-ray light curve of  $\eta$  Car showing the 2.0–10.0 keV flux as observed with NICER and eROSITA. The eRASS flux was scaled up by 30% to broadly match the NICER results taken from Espinoza-Galeas et al. (2022).

absorption, while  $kT$  and  $N_{\text{H}}$  are interdependent parameters in spectral modelling.

The eROSITA spectrum of  $\eta$  Car is predominantly of thermal origin, as shown in our model fits and evidenced by the strong Fe XXV 6.7 keV emission line. A fainter non-thermal contribution can always be hidden, especially in spectra with a moderate signal-to-noise ratio, because its basic spectral shape for reasonable values of the photon index is similar to those of a hot thermal plasma, but it is not required to adequately describe our data, nor is it favoured in the fits. On the other hand, non-thermal emission from  $\eta$  Car is detected at hard X-rays and soft Gamma-ray energies (Hamaguchi et al. 2018). However, the expected contribution is only at the percent level in the eROSITA energy range, which is consistent with our results and the conclusions from the spectral analysis.

#### 4.2. Wolf–Rayet stars

The CNC harbours three additional X-ray bright Wolf–Rayet stars, WR 22, WR 24, and WR 25, which are also eRASS sources. We discuss the data and summarise the spectral modelling results in Table 3.

**WR 25 (HD 93162).** This star is a massive colliding-wind binary of O2.5If\*/WN6+O type. It has component masses of about  $75+30 M_{\odot}$  and an orbital period of 208 days period, and it

has been studied in pointed X-ray observations (see e.g. Raassen et al. 2003; Gamen et al. 2006; Pollock & Corcoran 2006). In our survey data, WR 25 is the X-ray brightest of the Wolf–Rayet stars and the second brightest X-ray source in the studied Carina field after  $\eta$  Car. During eRASS, WR 25 was observed at orbital phases of 0.90, 0.77, 0.66, and 0.57, and its X-ray brightness varies by a factor of about two, as shown in Fig. 5. We measure an observed  $F_X = 3.3\text{--}6.9 \times 10^{-12} \text{ erg cm}^{-2} \text{ s}^{-1}$ , with the highest flux detected in the pre-periastron phase. However, changes in the spectral properties are minor, and except for a re-normalisation, a uniform spectral model is suitable to describe the data. We find an average  $\log L_X = 33.6$  and plasma components of comparable strength at temperatures of  $kT \approx 0.8$  and 2.0 keV.

**WR 22 (HD 92740).** The Wolf–Rayet star WR 22 is a WN7h+O9III-V system with  $70+25 M_{\odot}$  and  $P_{\text{orb}} = 80$  days. A discussion of the WR 22 system and a phase-resolved X-ray study with *XMM-Newton* is presented in Gosset et al. (2009). Over the eRASS, X-ray flux variations due to the orbital motion of about a factor of two are seen; see Fig. 5. The phase dependence (the eRASS1-4 phases are 0.59, 0.86, 0.15, and 0.50) of the observed rate is comparable to the rate observed with *XMM-Newton*. The spectra of WR 22 show a dominant 0.6–0.7 keV plasma component. In addition, we find indications for contributions from hotter plasma with  $kT \gtrsim 2.0 \text{ keV}$  as in WR 25, but this component is poorly constrained by our data.

**WR 24 (HD 93131).** WR 24 is a Wolf–Rayet star of spectral type WN6ha-w and the X-ray faintest of the studied WR stars. Its plasma temperature is comparable to the temperatures of WR 22, and similarly, indications for a hotter plasma component are present. These properties are quite typical for a colliding-wind binary, but no companion has been identified so far. While strong intrinsic absorption is seen in all WR stars, it is highest in WR 24.

#### 4.3. X-ray bright O stars

Other X-ray bright stellar sources are detected among the O-type stars. They are typically the more massive members with very strong stellar winds in a binary or a multiple system. An overview of the population of massive stars and a description of individual sources is given in Gagné et al. (2011), from where we adopted the stellar parameters when not denoted otherwise. We model and discuss the eRASS data from the most outstanding X-ray bright stellar sources in the following.



**Table 3.** Spectral fit results for eRASS:4 data.

Name	$N_{\text{H}}$ $10^{22}\text{cm}^{-2}$	$kT_1$ keV	$\log EM_1$ ( $\text{cm}^{-3}$ )	$kT_2$ keV	$\log EM_2$ ( $\text{cm}^{-3}$ )	$F_{\text{X}}$ $\text{erg cm}^{-2} \text{s}^{-1}$	$\log L_{\text{X}}$ ( $\text{erg s}^{-1}$ )
WR 22	$0.73^{+0.18}_{-0.19}$	$0.64^{+0.11}_{-0.13}$	$55.45^{+0.21}_{-0.22}$	–	–	$2.03\text{e-}13$	32.27
WR 24	$1.38^{+0.34}_{-0.24}$	$0.68^{+0.16}_{-0.17}$	$55.72^{+0.26}_{-0.21}$	–	–	$1.77\text{e-}13$	32.14
WR 25	$0.78^{+0.08}_{-0.10}$	$0.76^{+0.06}_{-0.05}$	$56.41^{+0.11}_{-0.14}$	$1.88^{+0.36}_{-0.22}$	$56.46^{+0.05}_{-0.06}$	$4.68\text{e-}12$	33.56
HD 93129/8	$0.23^{+0.07}_{-0.03}$	$0.85^{+0.08}_{-0.07}$	$55.44^{+0.12}_{-0.12}$	$3.79^{+2.75}_{-1.19}$	$55.95^{+0.07}_{-0.08}$	$1.93\text{e-}12$	33.25
HD 93160/1	$0.52^{+0.49}_{-0.30}$	$0.67^{+0.11}_{-0.15}$	$55.32^{+0.08}_{-0.08}$	–	–	$2.26\text{e-}13$	32.34
HD 93205	$0.20^{+0.10}_{+0.00}$	$0.13^{+0.30}_{-0.08}$	$55.13^{+2.16}_{-0.70}$	$0.74^{+0.20}_{-0.08}$	$55.12^{+0.06}_{-0.27}$	$3.32\text{e-}13$	32.78
HD 93206	$0.20^{+0.16}_{-0.00}$	$0.71^{+0.05}_{-0.11}$	$55.07^{+0.22}_{-0.12}$	$1.52^{+0.90}_{-0.30}$	$55.23^{+0.12}_{-0.15}$	$5.34\text{e-}13$	32.77
HD 93250	$0.20^{+0.08}_{-0.00}$	$0.80^{+0.07}_{-0.07}$	$55.19^{+0.13}_{-0.08}$	$4.48^{+11.7}_{-1.85}$	$55.67^{+0.08}_{-0.09}$	$1.10\text{e-}12$	33.03
HD 93403	$0.27^{+0.13}_{-0.07}$	$0.80^{+0.05}_{-0.05}$	$55.49^{+0.04}_{-0.04}$	$2.02^{+0.99}_{-0.37}$	$55.68^{+0.06}_{-0.06}$	$1.27\text{e-}12$	33.08
Coll 228-103	$0.20^{+0.00}_{-0.00}$	$0.27^{+0.25}_{-0.13}$	$54.72^{+0.31}_{-0.35}$	$1.14^{+0.33}_{-0.23}$	$54.73^{+0.15}_{-0.20}$	$1.57\text{e-}13$	32.34

**Notes.**  $F_{\text{X}}$  is the observed 0.2–5.0 keV flux, and  $L_{\text{X}}$  is the absorption-corrected 0.2–5.0 keV X-ray luminosity.  $N_{\text{H}}$  is the total column density, with the minimum value set to the mean ISM value. A two-temperature fit was used when it improved the fit significantly.

*HD 93129 (Trumpler 14-1).* The O-type star HD 93129 is one of the earliest-type stars in the Milky Way and a bright X-ray source. It was classified as an binary of the type O2If\*+O3.5V((f))5; but HD 93129 A was discovered to be a binary itself, consisting of an O2 supergiant and an O3.5 star, making HD 93129 a triple system at least. There is another massive binary HD 93128 (Trumpler 14-2) nearby, which is a spectroscopic binary of the spectral type O3.5V((fc)). Both stars are separated by 24 arcsec and are not fully resolved in the eRASS data, with HD 93129 being the dominant X-ray source by a factor of about four. Strong X-ray emission from hot plasma at  $kT$  of a few keV is detected from this source.

*HD 93160 and HD 93161.* These are O-type multiples of the spectral type O7III((f)) SB and O8V+O9V+O6.5(f) located in Trumpler 14. They are separated by 15 arcsec and blended in eRASS. The flux ratio of the two sources is about one, with HD 93161 being moderately brighter by 20%.

*HD 93205 (V560 Car).* It is an O-type binary of the spectral type O3.5V((f))+O8V. Its X-ray spectrum is one of the softest of the sources we studied, and we find that plasma at temperatures up to 1 keV dominates its X-ray emission.

*HD 93250.* It is an O4III(fc) star with suspected binarity, but a secondary was not unambiguously identified so far. The eRASS data confirm it as a bright X-ray source at  $L_{\text{X}} = 10^{33} \text{erg s}^{-1}$  with a strong hot plasma component at  $kT$  of a few keV.

*HD 93403.* It is an O5.5III(fc)+O7V eccentric binary. It is a bright X-ray source with  $L_{\text{X}} = 1.3 \times 10^{33} \text{erg s}^{-1}$  and has a hard X-ray spectrum that shows strong emission from hot plasma at  $kT$  of a few keV.

*HD 93206 (QZ Car).* It is located in Collinder 228 is a O9.7I+O8III double binary, that is, a quadruple system at least. Bright X-ray emission with a hot plasma component is observed from this massive O-type multiple system.

*Coll 228-103.* It is an OB star in the southern cluster Collinder 228, which is part of an OB mini-cluster consisting of Coll 228 101-103 and HD 305453.

The X-ray emission of the O-type stars we studied typically exhibits strong and often dominant plasma components at temperatures of about 0.6–0.8 keV. In addition, significant contributions from hotter plasma at a few keV are present in several targets. They are most prominent in HD 93129, HD 93206, HD 93250, and HD 93403, which all have  $kT_{\text{av}} \gtrsim 1$  keV. These high temperatures are specifically found in colliding-wind binaries or other multiple systems. In contrast, a few targets have predominantly cooler plasma in addition to the 0.6–0.8 keV component (HD 93205, Coll 228-103) and exhibit  $kT_{\text{av}} \lesssim 0.5$  keV in our models. Comparing the four eRASS visits for the O-type stars, we find only mild variability within about 20% in the observed X-ray fluxes. All spectral modelling results of the studied sources are summarised in Table 3.

## 5. Discussion

The CNC-Gum 31 region is a very bright H II region and a very active star-forming complex, but not as extreme as 30 Doradus (Dor) in the Large Magellanic Cloud (Massey & Hunter 1998) or the Arches cluster near the Galactic centre (Najarro et al. 2004). However, the close location of the CNC-Gum 31 complex and its properties make it an excellent target for the study of high-mass star-forming regions and therefore also for the understanding of the star formation in the early Universe.

### 5.1. Multi-wavelength comparison

In a new H I study at the Australia Telescope Compact Array, complex filamentary structures were found in the distribution of the cold neutral gas over a wide range of velocities (Rebolledo et al. 2017). Several bubbles were detected in the CNC, which have clearly been produced by the impact of the massive stars.

High-resolution observations of the  $^{12}\text{CO}(1-0)$  and  $^{13}\text{CO}(1-0)$  molecular lines in the Carina nebula and the Gum 31 region obtained with the 22 m Mopra telescope as part of The Mopra Southern Galactic Plane CO Survey were presented

by [Rebolledo et al. \(2016\)](#). From the sample of the massive clumps observed with Mopra, two regions with very different properties have been observed at the Atacama Large Millimeter/Submillimeter Array (ALMA) by [Rebolledo et al. \(2020\)](#). One region is located at the centre of the nebula and most likely experienced some feedback from the massive star clusters, while the other region was selected farther south and is thought to be less disturbed by the massive stars. It was shown that the centre of the nebula forms fewer cores than in the south, but the cores are much more massive. These differences suggest that stellar feedback has an effect on the formation of clumps that evolve into star-forming cores. In addition, [Fujita et al. \(2021\)](#) have analysed data taken with the Mopra and NANTEN2 telescopes as well as with ALMA and detected signatures of cloud-cloud collisions in the velocities and morphologies at different velocities of the clouds. They suggested that the collisions between clouds triggered massive star formation in CNC.

Moreover, the radio continuum map in the 1–3 GHz range ([Rebolledo et al. 2021](#)) shows a complex distribution of emission across the nebula, consisting of filaments, shells, and fronts on different size scales. Ionisation fronts are found at distances of 80 pc from the stellar clusters in the centre of the CNC to the north and south. It has been estimated that approximately 15% of the ionising flux has escaped from the nebula into the diffuse Galactic interstellar medium.

From the comparison of the radio continuum emission to the diffuse X-ray emission, we can conclude that the cavities seen in the H I map in the north and south were most likely formed by the influence of massive stars in the star clusters at the southern end of the northern cloud, as also confirmed by the bright diffuse X-ray emission in Central region C2. As pointed out by [Rebolledo et al. \(2021\)](#), the radio continuum and IR maps show plumes at the edges of the H II region, also around the northern tip of the X-ray hook. These plumes are indicative of cavities filled with over-pressurised hot gas that broke out and is expanding beyond the molecular cloud into the Galactic plane. The diffuse X-ray emission in the OS2 region is apparently due to the expanding hot plasma in the southern cavity.

## 5.2. Origin of the X-ray emission

The results of the spectral analysis indicate that the emission is mainly caused by thermal plasma in all regions. The element abundances are consistent with solar values, which indicates that the origin of the hot plasma is shocked ISM. [Townesley et al. \(2011a\)](#) found enhanced Fe abundance in their central arc region, which corresponds to our Hook region H1. In young stellar clusters such as those in the Carina nebula, it is likely that a supernova explosion occurred previously and that an SNR contributes to the X-ray emission. The combination of stellar winds and SNRs will create a superbubble around the stellar clusters. Therefore, in the context of the multi-wavelength study, we compare the observed emission with superbubble simulations ([Krause et al. 2013, 2014](#)).

The bright X-ray Hook region is most likely caused by a shock in a mixing region at the edge of a superbubble driven mainly by  $\eta$  Car. The time variability of the stellar driving power of superbubbles leads to various instabilities of superbubble shells, which tend to produce more extended turbulent mixing regions compared to the gradual change in density and temperature from the hot bubble interior to the dense shell, which would be expected from thermal conduction alone. Dissipation

in these mixing regions dominates the radiative losses in superbubbles (compare [Fierlinger et al. 2016](#)). In contrast to early 1D models with steady source power (e.g., [Chu & Mac Low 1990](#)), the losses can be strong enough and hence the internal energy density in the superbubble can be low enough for a significant increase in stellar source power to drive a shock wave through the entire superbubble. In the simulations of [Krause et al. \(2014\)](#), supernova shock waves encounter the optimal conditions in these mixing regions towards the inner edge of supershells to produce an enhancement on an order of magnitude in soft X-rays. In the present case, it seems likely that  $\eta$  Car, currently in the LBV phase, drives such a shock. An LBV phase is expected to last about  $10^5$  yr ([Groh et al. 2014](#)) with strong mass loss and powerful eruptive, possibly explosive winds ([Gormaz-Matamala et al. 2022; Vink 2022](#)). Winds of massive stars have typical velocities of about  $1000 \text{ km s}^{-1}$ . The distance of  $\sim 10$  pc between  $\eta$  Car and the X-ray hook are hence traversed in about  $10^4$  yr. It is therefore likely that the X-ray enhancement in the Hook region is caused by the current LBV phase of  $\eta$  Car.

The Central regions around  $\eta$  Car are best explained by the classical inner shock of its wind ([Weaver et al. 1977](#)). Due to strong adiabatic expansion, the temperature of the gas before the shock is low, and the shock Mach number is accordingly high. It is therefore highly likely that diffusive shock acceleration occurs at shocks like this ([Vink & Yamazaki 2014](#)). Consequently, we only find emission from non-thermal electrons in the regions around the massive stars, including  $\eta$  Car.

The radio continuum image ([Rebolledo et al. 2021](#)) suggests a superbubble around  $\eta$  Car, which is limited towards the south-east by the Hook region and extends significantly further towards the north-west. The latter is confirmed by the HI map in Fig. 2. Our Outer region O1 extends across a significant part of this superbubble, as defined by the radio continuum image, and is co-spatial with the radio continuum as well as with the *R*-band emission. The radio continuum and *R*-band image both show photoionised gas, which is found towards the inner edge of the superbubble shells.

The situation is different for our Outer region O2. There, the X-ray-bright region as well as the photoionised gas region is much narrower in the direction of the major axis of the corresponding superbubble (i.e. the one south of the Hook region). The X-rays here are anti-correlated with the photoionised gas, with X-rays being further inside the superbubble.

Our two Outer regions can be explained by hot gas being pushed against the shell of their respective superbubbles. The compression, and possibly some mixing, enhances the emission measure, and the regions are thus more prominent in X-rays. Southwards, the superbubble extends close to the plane of the sky. The comparatively denser part of the shell is photoionised. Hence, the X-rays appear to originate from inside the shell that is delineated by the photoionised gas, similar to the case of the Orion-Eridanus superbubble ([Krause et al. 2014](#)). The region O1 is seen almost from the top (or bottom), that is, the superbubble extends at a significant inclination to the plane of the sky. Hence, the X-ray-bright and radio continuum-bright regions appear to be overlaid.

The fact that we see the Outer regions O1 and O2 at similar X-ray brightness at the same time is probably accidental. As shown in [Krause et al. \(2014\)](#), the temporal variability of the stellar sources inside superbubbles leads to gas sloshing, that is, the hot gas moves around in superbubbles. The expected timescale of this variability is about  $10^5$  yr. Wherever the hot gas hits the dense shell, it becomes brighter due to the adiabatic

compression. This interpretation is consistent with the many arcs in the radio continuum image that are not associated with X-ray-bright regions. It is also possible that Outer region O1 is indicative of a temporal compression in the interior of the superbubble related to the gas sloshing.

The different bubbles around the individual massive star groups in the CNC are highly likely to have very different pressures. This follows from the strong dependence of the wind power on mass and evolutionary state of a star. The  $\eta$  Car bubble is clearly the highest-pressure system, which is not only evident from it having the most powerful stellar source,  $\eta$  Car, but also from the shock it drives, visible as the Hook region.

Due to the overpressure in the  $\eta$  Car bubble, a hot wind is driven through the molecular clouds in the centre of the system. The wind has swept away the more tenuous parts of the molecular cloud with which it is mixed southwards in our Outskirts regions. The mixing decreases the X-ray temperature and increases the emission measure, as observed. It is also interesting to compare the HI map (Fig. 2) to the molecular and radio continuum data (e.g., [Rebolledo et al. 2021](#), their Fig. 9). While the north-west superbubble and the southern superbubble seem connected in the HI map, molecular as well as ionised gas seems to be left in the interface between the two superbubbles. This might mean that the intermediate-density gas (HI) is blown away and mixed into the X-ray gas, whereas the denser, molecular parts remain. Some of the dense gas is photoionised and continues to be ablated.

The denser gas in the molecular clouds, which is not swept away, is likely to be surrounded by the hot X-ray gas and compressed by its high pressure (compare [Krause et al. 2018](#)). This may well be the mechanism that formed the massive cores detected by ALMA in the central part of the nebula (compare above). This process has been suggested to explain the sequential star formation in the Scorpius-Centaurus superbubble by [Krause et al. \(2018\)](#). Their simulations directly support the combination of sweeping away more tenuous gas with the formation of dense gas cores. The plumes identified in the radio continuum image are also consistent with this picture and probably represent somewhat denser gas phases that are pushed out of the molecular region by the hot wind.

### 5.3. Thermal properties of the superbubble

If the high-mass stars in the Central region blow strong stellar winds and encounter an obstacle in the X-ray hook, these regions should have a higher pressure than the surroundings. We used the results from the X-ray spectral analysis to estimate the density and pressure in these regions.

We assumed that in the Central region, the stars blow a bubble with a size similar to Central regions C1 and C2. We approximated the bubble as a sphere with a diameter of  $0.37^\circ$ . The Hook region (H1 and H2) is most likely a shell-like structure around the Central region that we see from the side. We assumed that it can be modelled as a part of a spherical shell with an outer diameter of  $1^\circ$  and an inner diameter of  $0.65^\circ$ . We also studied Outskirt region OS2, which is plasma flowing into the northern part of the southern cavity. We modelled the structure as a half-ellipsoid with a major axis  $a$  of  $0.64^\circ$  and a minor axis  $b$  of  $0.5^\circ$ . For the axis parallel to our line of sight  $c$ , we assumed the same value as for the minor axis  $b$ .

Based on these assumptions, we calculated the following volumes for the X-ray emission: for the Central regions (C1 and C2)  $V_c = 4.2 \times 10^{58} \text{ cm}^3$ , for the Hook regions (H1 and H2)  $V_h = 2.9 \times 10^{59} \text{ cm}^3$ , and for region OS2  $V_{os} = 5.8 \times 10^{59} \text{ cm}^3$ .

To calculate the density, we used the normalisation of the spectral models for thermal plasma,

$$\text{norm}_i = \frac{10^{-14}}{4\pi D^2} \int n_e n_H dV = \frac{10^{-14}}{4\pi D^2} 1.2 n_H^2 V_i, \quad (1)$$

with  $D$  being the distance to the CNC, and assuming homogeneous density in each of the regions and  $n_e = 1.2 n_H$ . The index  $i = c, h,$  and  $os$  denotes the parameters for the Central regions (combined), the Hook regions (combined), or region OS2. For the hydrogen density and the pressure of the plasma, we therefore obtain

$$n_{H,i} = \sqrt{\frac{4\pi D^2 \text{norm}_i}{1.2 \times 10^{-14} V_i}} \quad (2)$$

and

$$P_i/k = (n_{e,i} + n_{H,i} + n_{\text{others},i})T = (1.2 + 1.1)n_{H,i}T_i. \quad (3)$$

Using Eqs. (2) and (3), we obtain for the Central regions  $n_{H,c} = 4.0 \times 10^{-2} \text{ cm}^{-3}$  and  $P_c/k = 9.1 \times 10^5 \text{ cm}^{-3} \text{ K}$ , for the Hook regions  $n_{H,h} = 5.4 \times 10^{-2} \text{ cm}^{-3}$  and  $P_h/k = 9.4 \times 10^5 \text{ cm}^{-3} \text{ K}$ , and for region OS2  $n_{H,os} = 2.3 \times 10^{-2} \text{ cm}^{-3}$  and  $P_{os}/k = 5.1 \times 10^5 \text{ cm}^{-3} \text{ K}$ . The uncertainties on the temperature and the normalisation are about 5% and 10%, respectively, while our volume estimate is most likely uncertain by 20–30%. Therefore, the derived values have an uncertainty of  $\sim 50\%$ . The numbers still indicate that the density and pressure are higher in the Central and Hook regions, while the lower pressure in the southern cavity indicates outflowing gas. The pressure in the CNC is higher by one to two orders of magnitude than the average pressure in the ISM in the Milky Way ([Jenkins & Tripp 2021](#), and references therein).

### 5.4. Cosmic-ray pressure

In the shocks of the strong stellar winds of massive stars, electrons and protons are accelerated to relativistic energies and become cosmic rays. In young stellar clusters such as the Carina nebula, there also regions in which stellar winds collide and that are therefore very efficient acceleration regions (see, e.g., [Steinmassl et al. 2023](#), and references therein). The harder emission in the spectrum in the Central regions can either be explained by synchrotron radiation or by inverse Compton scattering of the accelerated particles.

For the synchrotron hypothesis, we need to assume a magnetic field strength. As the thermal pressure is higher by about two orders of magnitude than the Galactic average, we might expect a similarly enhanced magnetic pressure. Because the magnetic field in the Milky Way is generally about  $\mu\text{G}$  ([Sun & Reich 2010](#); [Xu & Han 2019](#); [Dickey et al. 2022](#)), we may expect a magnetic field in the Carina superbubble system of several  $10 \mu\text{G}$ . The synchrotron emissivity for a power-law distribution of electrons is given by ([Longair 2011](#))

$$J(\nu) = A \frac{\sqrt{3\pi} e^3 B}{16\pi^2 \epsilon_0 m_e c (q-1) \kappa} \left( \frac{2\pi \nu m_e^3 c^4}{3eB} \right)^{-\frac{q-1}{2}} \quad (4)$$

with

$$A = \frac{\Gamma_f\left(\frac{q}{4} + \frac{19}{12}\right) \Gamma_f\left(\frac{q}{4} - \frac{1}{12}\right) \Gamma_f\left(\frac{q}{4} + \frac{5}{4}\right)}{\Gamma_f\left(\frac{q}{4} + \frac{7}{12}\right)}. \quad (5)$$



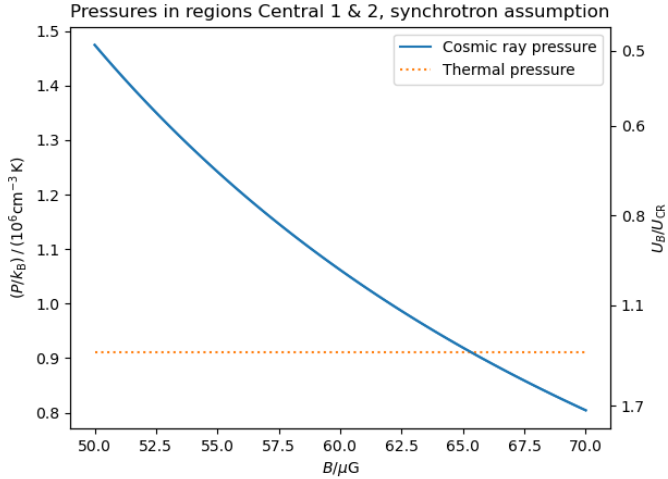


**Fig. 8.** Possible cosmic-ray pressure in regions C1 and C2 under the assumption that the measured non-thermal X-ray radiation is synchrotron emission. The blue line shows the total cosmic-ray pressure (hadrons + leptons, left vertical axis) and the ratio of the magnetic and total cosmic-ray pressure (right vertical axis) over magnetic field strength. The magnetic field values we used are not observationally known, but are reasonable values given other observables of the region. The orange line shows the thermal pressure of the same region for comparison (left axis). See Sect. 5.4 for a discussion of this plot.

Here,  $m_e$  and  $e$  are the electron mass and charge, respectively,  $c$  is the speed of light, and  $\epsilon_0$  is the vacuum permittivity. The Gamma function is denoted by  $\Gamma_f$ , and the electron energy distribution is  $n(E) = \kappa E^{-q}$ . The electron distribution power-law index  $q$  is related to the photon index  $\Gamma$  by  $q = 2\Gamma - 1$ . For an assumed magnetic field strength  $B$ , the characteristic frequency for synchrotron emission is given by

$$\nu_c = 7 \times 10^{17} \text{ Hz} \left( \frac{E}{30 \text{ TeV}} \right)^2 \left( \frac{B}{\text{nT}} \right). \quad (6)$$

The non-thermal luminosity observed in the X-ray band is given by the integral  $\int_{\nu_1}^{\nu_2} J(\nu) d\nu$ , and we took  $\nu_1 = 4.5 \text{ keV h}^{-1}$  and  $\nu_2 = 12 \text{ keV h}^{-1}$  to be clearly dominated by the non-thermal part of the spectrum. This procedure allows us to infer  $\kappa$  for an assumed magnetic field by equating the predicted luminosity to the non-thermal luminosity we observe in regions Central 1 and 2,  $L_{\text{obs,nt,4.5-12 keV}} = 5.59 \times 10^{33} \text{ erg s}^{-1}$ , which we used to infer the relativistic electron pressure by integrating over the energy distribution,

$$P_{\text{cr,e}} = (\gamma_{\text{ad}} - 1) \int_{E_1}^{E_2} E n(E) dE, \quad (7)$$

where the adiabatic index is  $\gamma_{\text{ad}} = 4/3$  for relativistic particles. We followed del Palacio et al. (2022) in adopting a leptonic contribution to the overall cosmic-ray pressure of 2%.

The cosmic-ray pressure as well as the ratio of the magnetic and the cosmic-ray pressure are shown over the assumed magnetic field strength in Fig. 8. The thermal pressure is also shown for comparison. Under the synchrotron hypothesis, our measurements allow for two possible solutions: if the magnetic field strength is low, the region must be dominated by the cosmic-ray pressure. If the magnetic field is high, magnetic pressure will dominate. The measurements exclude the possibility that the thermal pressure dominates. A solution with all three pressure

components in approximate equipartition exists for  $B \approx 60 \mu\text{G}$ . We note that for these assumptions, we predict a non-thermal radio flux at 2 GHz of 7 Jy, which is well consistent with the thermally dominated radio continuum emission of 2 kJy observed by (Rebolledo et al. 2021). There are generally very few detections of non-thermal radio components in superbubbles, and it is possible that special geometries or circumstances may be required to distinguish the non-thermal contributions (compare Heesen et al. 2015).

Strong magnetic field amplification is expected for shocks that produce the high-energy leptons (up to about 30 TeV) required in the synchrotron hypothesis (Schure et al. 2012; Vink 2012). The physics could be similar to the situation in the 30 Dor superbubble (Kavanagh et al. 2019), where TeV emission of the high-energy lepton population may be observed, but in the present case, the accelerating shock would be the terminal wind shocks of the massive stars in the Central regions. Gamma-rays up to at least 400 GeV are also observed from the direction of  $\eta$  Car (Abdo et al. 2010; Martí-Devesa & Reimer 2021; H.E.S.S. Collaboration 2020; Steinmassl et al. 2023). Given the extent of the point spread function in the HESS detection, some of this emission might be related to any inverse Compton component of the hypothetical TeV electrons, although the correlation of the GeV emission with the orbital period of  $\eta$  Car observed with *Fermi* (Martí-Devesa & Reimer 2021) and the detection of the colliding-wind binary in hard X-rays with NuSTAR associate the bulk of this high-energy emission directly with  $\eta$  Car (Hamaguchi et al. 2018). The GeV  $\gamma$ -ray emission observed with *Fermi* (Abdo et al. 2010; Martí-Devesa & Reimer 2021) could also receive a contribution from leptonic emission (H.E.S.S. Collaboration 2020), but seems to be at least partly due to pion decay caused by the interaction of a hadronic cosmic-ray population with the dense gas in the region (Ge et al. 2022).

The possible non-thermal X-ray spectrum we detect could be caused by inverse Compton upscattering of starlight or photons from the cosmic microwave background (CMB) by relativistic electrons with much lower Lorentz factors. The frequency shift is approximately given by (Longair 2011):

$$\frac{E_{\text{IC}}}{5 \text{ keV}} = \left( \frac{\gamma}{30} \right)^2 \left( \frac{400 \text{ nm}}{\lambda} \right) = \left( \frac{\gamma}{2000} \right)^2 \left( \frac{\nu}{160 \text{ GHz}} \right). \quad (8)$$

Hence, upscattering from optical or UV (wavelength  $\lambda \approx 400 \text{ nm}$ ) to X-rays requires electrons with Lorentz factors of  $\gamma \approx 30$ . From the direct measurements of the local cosmic-ray electron population at MeV energies, we know that the energy spectrum becomes very flat,  $q \approx 1.4$  (after accounting for the solar modulation, Orlando 2018; Vittino et al. 2019; Krause & Hardcastle 2021). If the situation were similar in the CNC, we would expect a non-thermal photon index of around 1.2 rather than the 1.8 that we observe. We estimated the cosmic-ray pressure for this case in the following way: for a radiation energy density  $U_{\text{rad}}$ , the inverse Compton luminosity is given by (Longair 2011)

$$L_{\text{IC}} = \frac{4}{3} \gamma^2 \sigma_{\text{T}} c U_{\text{rad}} N_e, \quad (9)$$

with the Thompson cross section  $\sigma_{\text{T}}$  and the number of upscattering electrons  $N_e$ . The latter can then be obtained by equating  $L_{\text{IC}}$  to the observed luminosity. The total cosmic-ray pressure for the same assumptions as above is then given by

$$P_{\text{CR}} = (\gamma_{\text{ad}} - 1) \frac{51 N_e \gamma m_e c^2}{V}. \quad (10)$$

Smith (2006) gives a luminosity in ionising photons of  $Q = 10^{51} \text{ s}^{-1}$ , corresponding to a photon density of a few photons per  $\text{cm}^3$  or  $U_{\text{rad}} \approx 10^{-11} \text{ erg cm}^{-3}$ . This would yield a cosmic-ray pressure of  $P_{\text{CR}}/k \approx 10^9 \text{ cm}^{-3} \text{ K}$ , which is much higher than what we would expect in this region (compare above).

The CMB peaks at a frequency of  $\nu = 160 \text{ GHz}$  and has an energy density of  $U_{\text{rad}} = 4 \times 10^{13} \text{ erg cm}^{-3}$ . An analysis similar as before yields an estimate of the total cosmic-ray pressure of  $P_{\text{CR}}/k \approx 10^9 \text{ cm}^{-3} \text{ K}$ , which is similar to the above estimate and again much higher than the thermal pressure that we derived above.

In conclusion, if the non-thermal spectrum in the Central regions were due to inverse Compton scattering, the pressure in the region would be strongly dominated by cosmic rays even if only the leptonic component were taken into account. These considerations seem to favour the synchrotron hypothesis. More sensitive TeV observations might be able to confirm or refute this.

As a further consistency check, we can determine the radius of the termination (inner) shock of the combined wind from the  $\eta$  Car binary. We adopted the values collected in Groh et al. (2012, see Table 4). Here,  $\rho$  is the wind density and  $v$  is the velocity of the wind, and the wind ram pressure equals the ambient pressure  $p = \rho v^2$  at the termination shock. We took the thermal pressure in the Central region as proxy for the ambient pressure. With this assumption, we find for the radius of the termination shock,

$$r_{\text{ts}} = \left( \frac{L\dot{M}}{8\pi^2 p^2} \right)^{1/4} = 15 \text{ pc} \left( \frac{L}{L_c} \right)^{1/4} \left( \frac{\dot{M}}{\dot{M}_c} \right)^{1/4} \left( \frac{p}{P_c} \right)^{-1/2}. \quad (11)$$

Given the evidence for the additional cosmic-ray pressure, we expect a termination shock somewhat closer to  $\eta$  Car than 15 pc, which is consistent with our assumption above that this shock accelerates the non-thermal particles to TeV energies in the Central regions, and it is consistent with the synchrotron hypothesis above. For this magnitude of the termination shock radius, it is possible that the shock has traversed the entire distance between  $\eta$  Car and the denser gas in the Hook region.

### 5.5. Comparison of the X-ray luminosity to the wind power

The X-ray emission arises in the shock-heated intermediate-density gas and due to mixing between the hotter, shocked ejecta and the denser and colder gas phases. The X-ray luminosity can increase sharply after a strong energy increase; an increase of up to a factor of several dozen is seen after a supernova in the superbubble, which then decays over about  $10^5$  yr, as shown by Krause et al. (2014). The simulations predict that about  $2\text{--}3 \times 10^{-4}$  of the kinetic power injected by massive stars will be emitted in the 0.2–12 keV band on average, and a fraction of about  $10^{-6}$  in the 2–4.5 keV band.

The current kinetic power output by massive stars in the CNC was estimated by Smith (2006) to be  $L_{\text{kin}} = 3.4 \times 10^{38} \text{ erg s}^{-1}$ . We collect partly updated estimates from the literature in Table 4 for the stars we detect in X-rays, which, by comparison to Smith (2006), probably contribute the bulk of the kinetic power. Some values have increased in more recent analyses. For our sample alone, we already find a combined wind power of  $L_{\text{kin}} = 3.6 \times 10^{38} \text{ erg s}^{-1}$ .

We derived a thermal X-ray luminosity of the entire CNC of  $1.31 \times 10^{35} \text{ erg s}^{-1}$  (0.2–12 keV), or about  $\lesssim 3 \times 10^{-4}$  of the wind power. This is for our adopted assumption for the foreground absorption (without this, the values would be higher by about

**Table 4.** Properties of some massive-star winds in the CNC.

Name	$\dot{M}/10^{-5}$ $M_{\odot} \text{ yr}^{-1}$	$v_{\infty}$ $\text{km s}^{-1}$	$L_{\text{kin}}/10^{37}$ $\text{erg s}^{-1}$	Refs.
$\eta$ Car A	85	420	4.8	1
$\eta$ Car B	2	3000	5.7	1
WR 22	1.9	1785	1.9	2, 3
WR 24	3.4	2160	5.0	2
WR 25A	2.5	2480	4.9	4
WR 25B	0.25	2250	0.40	4
HD 93128	0.45	3355	1.6	5
HD 93129Aa	2.0	3200	6.5	5
HD 93129Ab	0.61	3200	0.52	5
HD 93129B	0.45	3355	1.6	5
HD 93160	0.22	2560	0.46	6
HD 93160	0.22	2560	0.46	6
HD 93161Aa	0.026	2100	0.036	6
HD 93161Ab	0.018	1820	0.019	6
HD 93161B	0.06	2460	0.12	6
HD 93205A	0.25	3080	0.75	6
HD 93205B	0.026	2100	0.036	6
HD 93206A	0.19	1510	0.14	6
HD 93206B	0.05	1820	0.053	6
HD 93250	0.056	3160	0.18	7, 8
HD 93403A	0.34	2760	0.82	6
HD 93403B	0.04	2320	0.068	6
Total			35.6	

**References.** 1: Groh et al. (2012), 2: Hamann et al. (2006), 3: Lenoir-Craig et al. (2022), 4: Pradhan et al. (2021), 5: Rainot et al. (2022), 6: Smith (2006), 7: Prinja et al. (1990), 8: Nebot Gómez-Morán & Oskinova (2018).

40%). This compares very well to the predictions of Krause et al. (2014). In the 2–4.5 keV band, we measure a thermal X-ray luminosity of  $2.35 \times 10^{33} \text{ erg s}^{-1}$ , which corresponds to a fraction of  $\lesssim 7 \times 10^{-6}$  of the wind power. This again agrees reasonably well with the prediction from the 3D superbubble simulations, and it indicates that the thermal structure in the emerging Carina superbubble is similar to the structure in the simulations.

A comparison between Table 4 and Fig. 4 confirms that the strongest stellar winds are from the  $\eta$  Car binary and the surrounding stars, and that the gas dynamics observed in X-rays in the CNC is thus indeed driven by this region.

## 6. Summary

We have analysed the diffuse X-ray emission in the CNC observed in four all-sky surveys with eROSITA (eRASS:4). The complete coverage of the CNC and its surroundings with eROSITA has allowed us to constrain the local X-ray background emission in a more improved way than in the studies before, and we obtained reliable fit results of the X-ray spectra. We created images in X-rays, which were compared to multi-wavelength images, in particular with HI data, to identify cavities in the cold ISM. These cavities have most likely been created by the winds of the massive stars and are filled with hot X-ray emitting, low-density plasma. In all regions, the dominating emission is modelled best as emission from thermal plasma. Near the massive stars, in particular,  $\eta$  Car, an additional non-thermal emission component is detected in the X-ray spectrum.

The most prominent feature in the CNC in X-rays is the V-shaped X-ray hook, which is anti-correlated with the bright triangular shape of photoionised gas seen in the optical. As the spectral analysis of the eROSITA data have shown, in the X-ray bright Hook region H1, located south of the massive stars, the emission of the hot plasma component is stronger than in other regions. In this part of the nebula, the ionisation timescale is also high, suggesting high density, which is also consistent with the high brightness. The X-ray hook is most likely the edge of a superbubble formed by the shocks of the stellar winds of massive stars, mainly by  $\eta$  Car. The fainter, more diffuse emission in the Outer regions is caused by the hot gas that fills the superbubbles around the massive stars in the CNC. The pressure inside the superbubbles, as derived from the spectral fit parameters, is one to two orders of magnitude higher than in the ISM. We suggest that the Outer regions result from mixing of the hot gas driven by an overpressure in the Central regions through the cold filamentary gas in the Hook region, with the ablated cold gas.

The spectrum in the centre of the CNC is harder than in the Outer regions, indicating that there is either an additional hot thermal emission, as found by Townsley et al. (2011a), or a non-thermal component. The latter is favoured in the fit of the eRASS:4 spectrum in the region around  $\eta$  Car and can be explained as synchrotron emission from electrons accelerated in enhanced magnetic fields inside the CNC. From the photon index and the flux obtained from X-ray spectrum, we derived the energy distribution and the pressure of the electron gas and a magnetic field strength of  $B \approx 60 \mu\text{G}$  assuming equipartition. The theoretical size of the termination shock around  $\eta$  Car is very much consistent with the distance of the X-ray hook from  $\eta$  Car. The luminosity of the diffuse X-ray emission in the entire Carina nebula is about  $10^{35} \text{ erg s}^{-1}$  (0.2–12 keV), which is consistent with the luminosity of the diffuse emission obtained with *Chandra* (Townsley et al. 2011b) and expectations from superbubble simulations (Krause et al. 2014).

We have also studied the X-ray emission from the massive stars and binaries in the Carina nebula, in particular the LBV binary  $\eta$  Car and the Wolf-Rayet stars WR 22, WR 24, and WR 25, and bright O stars. Their X-ray spectra are well modelled with one or two components of thermal plasma emission, with relatively high temperatures ( $kT > 0.6 \text{ keV}$ ). The data of the four surveys show variation in the X-ray flux with orbital phase for  $\eta$  Car, WR 22, and WR 25.  $\eta$  Car was observed shortly before periastron in eRASS1, with brighter emission above 1 keV. This harder variable emission can be explained as emission from the wind-wind collision zone in the binary.

**Acknowledgements.** In fond memory of Dr. Leisa Townsley. This work is based on data from eROSITA, the soft X-ray instrument aboard SRG, a joint Russian-German science mission supported by the Russian Space Agency (Roskosmos), in the interests of the Russian Academy of Sciences represented by its Space Research Institute (IKI), and the Deutsches Zentrum für Luft- und Raumfahrt (DLR). The SRG spacecraft was built by Lavochkin Association (NPOL) and its subcontractors, and is operated by NPOL with support from the Max Planck Institute for Extraterrestrial Physics (MPE). The development and construction of the eROSITA X-ray instrument was led by MPE, with contributions from the Dr. Karl Remeis Observatory Bamberg & ECAP (FAU Erlangen-Nürnberg), the University of Hamburg Observatory, the Leibniz Institute for Astrophysics Potsdam (AIP), and the Institute for Astronomy and Astrophysics of the University of Tübingen, with the support of DLR and the Max Planck Society. The Argelander Institute for Astronomy of the University of Bonn and the Ludwig Maximilians Universität Munich also participated in the science preparation for eROSITA. The eROSITA data shown here were processed using the eSASS/NRTA software system developed by the German eROSITA consortium. The Digitized Sky Surveys were produced at the Space Telescope Science Institute under US Government grant NAG W-2166. The images of these surveys are based on photographic data obtained using the Oschin Schmidt Telescope on Palomar Mountain and the UK Schmidt Telescope. The plates were processed

into the present compressed digital form with the permission of these institutions. M.S. acknowledges support from the Deutsche Forschungsgemeinschaft through the grants SA 2131/13-1, SA 2131/14-1, and SA 2131/15-1. J.R. acknowledges support from the DLR under grant 50QR2105.

## References

- Abdo, A. A., Ackermann, M., Ajello, M., et al. 2010, *ApJ*, 723, 649  
 Borkowski, K. J., Lyerly, W. J., & Reynolds, S. P. 2001, *ApJ*, 548, 820  
 Brooks, K. J., Whiteoak, J. B., & Storey, J. W. V. 1998, *PASA*, 15, 202  
 Brunner, H., Liu, T., Lamer, G., et al. 2022, *A&A*, 661, A1  
 Cappellari, M., & Copin, Y. 2003, *MNRAS*, 342, 345  
 Castor, J., McCray, R., & Weaver, R. 1975, *ApJ*, 200, L107  
 Chu, Y.-H., & Mac Low, M.-M. 1990, *ApJ*, 365, 510  
 Corcoran, M. F., Rawley, G. L., Swank, J. H., & Petre, R. 1995, *ApJ*, 445, L121  
 Corcoran, M. F., Ishibashi, K., Swank, J. H., & Petre, R. 2001, *ApJ*, 547, 1034  
 Corcoran, M. F., Liburd, J., Morris, D., et al. 2017, *ApJ*, 838, 45  
 Corcoran, M. F., Hamaguchi, K., Smith, N., et al. 2022, *ApJ*, 937, 122  
 Cox, P., & Bronfman, L. 1995, *A&A*, 299, 583  
 del Palacio, S., Benaglia, P., De Becker, M., Bosch-Ramon, V., & Romero, G. E. 2022, *PASA*, 39, e004  
 Dennerl, K., Andritschke, R., Bräuninger, H., et al. 2020, *SPIE Conf. Ser.*, 11444, 114444Q  
 Dickey, J. M., West, J., Thomson, A. J. M., et al. 2022, *ApJ*, 940, 75  
 Doi, Y., Takita, S., Ootsubo, T., et al. 2015, *PASJ*, 67, 50  
 Espinoza-Galeas, D., Corcoran, M. F., Hamaguchi, K., et al. 2022, *ApJ*, 933, 136  
 Ezoë, Y., Hamaguchi, K., Gruendl, R. A., et al. 2009, *PASJ*, 61, S123  
 Fierlinger, K. M., Burkert, A., Ntormousi, E., et al. 2016, *MNRAS*, 456, 710  
 Freyberg, M., Perinati, E., Pacaud, F., et al. 2020, *SPIE Conf. Ser.*, 11444, 114441O  
 Fujita, S., Sano, H., Enokiya, R., et al. 2021, *PASJ*, 73, S201  
 Gagné, M., Fehon, G., Savoy, M. R., et al. 2011, *ApJS*, 194, 5  
 Gamen, R., Gosset, E., Morrell, N., et al. 2006, *A&A*, 460, 777  
 Ge, T.-T., Sun, X.-N., Yang, R.-Z., Liang, Y.-F., & Liang, E.-W. 2022, *MNRAS*, 517, 5121  
 Göppel, C., & Preibisch, T. 2022, *A&A*, 660, A11  
 Gormaz-Matamala, A. C., Curé, M., Meynet, G., et al. 2022, *A&A*, 665, A133  
 Gosset, E., Nazé, Y., Sana, H., Rauw, G., & Vreux, J. M. 2009, *A&A*, 508, 805  
 Groh, J. H., Hillier, D. J., Madura, T. I., & Weigelt, G. 2012, *MNRAS*, 423, 1623  
 Groh, J. H., Meynet, G., Ekström, S., & Georgy, C. 2014, *A&A*, 564, A30  
 Hamaguchi, K., Corcoran, M. F., Gull, T., et al. 2007a, *ApJ*, 663, 522  
 Hamaguchi, K., Petre, R., Matsumoto, H., et al. 2007b, *PASJ*, 59, 151  
 Hamaguchi, K., Corcoran, M. F., Pittard, J. M., et al. 2018, *Nat. Astron.*, 2, 731  
 Hamann, W. R., Gräfener, G., & Liermann, A. 2006, *A&A*, 457, 1015  
 Heesen, V., Brinks, E., Krause, M. G. H., et al. 2015, *MNRAS*, 447, L1  
 H. E. S. S. Collaboration (Abdalla, H., et al.) 2020, *A&A*, 635, A167  
 HI4PI Collaboration (Ben Bekhti, N., et al.) 2016, *A&A*, 594, A116  
 Jenkins, E. B., & Tripp, T. M. 2021, *ApJ*, 916, 17  
 Kalberla, P. M. W., & Haud, U. 2015, *A&A*, 578, A78  
 Kalberla, P. M. W., McClure-Griffiths, N. M., Pisano, D. J., et al. 2010, *A&A*, 521, A17  
 Kashi, A., & Soker, N. 2016, *ApJ*, 825, 105  
 Kavanagh, P. J., Vink, J., Sasaki, M., et al. 2019, *A&A*, 621, A138  
 Kavanagh, P. J., Sasaki, M., Breitschwerdt, D., et al. 2020, *A&A*, 637, A12  
 Kerp, J., Winkel, B., Ben Bekhti, N., Flöer, L., & Kalberla, P. M. W. 2011, *Astron. Nachr.*, 332, 637  
 Kharchenko, N. V., Piskunov, A. E., Röser, S., Schilbach, E., & Scholz, R. D. 2005, *A&A*, 438, 1163  
 Krause, M. G. H., & Hardcastle, M. J. 2021, *MNRAS*, 502, 2807  
 Krause, M., Fierlinger, K., Diehl, R., et al. 2013, *A&A*, 550, A49  
 Krause, M., Diehl, R., Böhringer, H., Freyberg, M., & Lubos, D. 2014, *A&A*, 566, A94  
 Krause, M. G. H., Burkert, A., Diehl, R., et al. 2018, *A&A*, 619, A120  
 Kuntz, K. D., & Snowden, S. L. 2010, *ApJS*, 188, 46  
 Lenoir-Craig, G., Antokhin, I. I., Antokhina, E. A., St-Louis, N., & Moffat, A. F. J. 2022, *MNRAS*, 510, 246  
 Longair, M. S. 2011, *High Energy Astrophysics* (Cambridge University Press)  
 Martí-Devesa, G., & Reimer, O. 2021, *A&A*, 654, A44  
 Massey, P., & Hunter, D. A. 1998, *ApJ*, 493, 180  
 McClure-Griffiths, N. M., Pisano, D. J., Calabretta, M. R., et al. 2009, *ApJS*, 181, 398  
 Merloni, A., Predehl, P., Becker, W., et al. 2012, *ArXiv e-prints* [arXiv:1209.3114]  
 Merloni, A., Liu, T., Ramos-Ceja, M. E., et al. 2024, *A&A*, in press, <https://doi.org/10.1051/0004-6361/202347165>  
 Najarro, F., Figer, D. F., Hillier, D. J., & Kudritzki, R. P. 2004, *ApJ*, 611, L105



- Nazé, Y., Broos, P. S., Oskinova, L., et al. 2011, *ApJS*, 194, 7
- Nebot Gómez-Morán, A., & Oskinova, L. M. 2018, *A&A*, 620, A89
- Orlando, E. 2018, *MNRAS*, 475, 2724
- Pittard, J. M., & Corcoran, M. F. 2002, *A&A*, 383, 636
- Pollock, A. M. T., & Corcoran, M. F. 2006, *A&A*, 445, 1093
- Povich, M. S., Smith, N., Majewski, S. R., et al. 2011, *ApJS*, 194, 14
- Pradhan, P., Huenemoerder, D. P., Ignace, R., Pollock, A. M. T., & Nichols, J. S. 2021, *ApJ*, 915, 114
- Predehl, P., Andritschke, R., Arefiev, V., et al. 2021, *A&A*, 647, A1
- Preibisch, T., Ratzka, T., Kuderna, B., et al. 2011a, *A&A*, 530, A34
- Preibisch, T., Schuller, F., Ohlendorf, H., et al. 2011b, *A&A*, 525, A92
- Preibisch, T., Roccatagliata, V., Gaczkowski, B., & Ratzka, T. 2012, *A&A*, 541, A132
- Prinja, R. K., Barlow, M. J., & Howarth, I. D. 1990, *ApJ*, 361, 607
- Raassen, A. J. J., van der Hucht, K. A., Mewe, R., et al. 2003, *A&A*, 402, 653
- Rainot, A., Reggiani, M., Sana, H., Bodensteiner, J., & Absil, O. 2022, *A&A*, 658, A198
- Rebolledo, D., Burton, M., Green, A., et al. 2016, *MNRAS*, 456, 2406
- Rebolledo, D., Green, A. J., Burton, M., et al. 2017, *MNRAS*, 472, 1685
- Rebolledo, D., Guzmán, A. E., Contreras, Y., et al. 2020, *ApJ*, 891, 113
- Rebolledo, D., Green, A. J., Burton, M. G., Breen, S. L., & Garay, G. 2021, *ApJ*, 909, 93
- Schure, K. M., Bell, A. R., O’C Drury, L., & Bykov, A. M. 2012, *Space Sci. Rev.*, 173, 491
- Seward, F. D., & Chlebowski, T. 1982, *ApJ*, 256, 530
- Shull, J. M., Darling, J., & Danforth, C. W. 2021, *ApJ*, 914, 18
- Smith, N. 2006, *MNRAS*, 367, 763
- Smith, N. & Brooks, K. J. 2008, in *Handbook of Star Forming Regions, Vol. II: The Southern Sky*, ed. B. Reipurth, ASP Monograph Publ., 5, 138
- Smith, N., Egan, M. P., Carey, S., et al. 2000, *ApJ*, 532, L145
- Smith, N., Povich, M. S., Whitney, B. A., et al. 2010, *MNRAS*, 406, 952
- Steinmassl, S., Breuhaus, M., White, R., Reville, B., & Hinton, J. A. 2023, *A&A*, 679, A118
- Sun, X.-H., & Reich, W. 2010, *Res. Astron. Astrophys.*, 10, 1287
- Townsley, L. K., Broos, P. S., Chu, Y.-H., et al. 2011a, *ApJS*, 194, 15
- Townsley, L. K., Broos, P. S., Chu, Y.-H., et al. 2011b, *ApJS*, 194, 16
- Townsley, L. K., Broos, P. S., Corcoran, M. F., et al. 2011c, *ApJS*, 194, 1
- Vink, J. 2012, *A&ARv.*, 20, 49
- Vink, J. S. 2022, *ARA&A*, 60, 203
- Vink, J., & Yamazaki, R. 2014, *ApJ*, 780, 125
- Vittino, A., Mertsch, P., Gast, H., & Schael, S. 2019, *Phys. Rev. D*, 100, 043007
- Weaver, R., McCray, R., Castor, J., Shapiro, P., & Moore, R. 1977, *ApJ*, 218, 377
- Whiteoak, J. B., & Otrupcek, R. E. 1984, *PASA*, 5, 552
- Wilms, J., Allen, A., & McCray, R. 2000, *ApJ*, 542, 914
- Winkel, B., Kerp, J., Flöer, L., et al. 2016, *A&A*, 585, A41
- Xu, J., & Han, J. L. 2019, *MNRAS*, 486, 4275
- Yeung, M. C. H., Freyberg, M. J., Ponti, G., et al. 2023, *A&A*, 676, A3
- Yonekura, Y., Asayama, S., Kimura, K., et al. 2005, *ApJ*, 634, 476

**Appendix A: eRASS catalogue entries****Table A.1.** eRASS1-data release 1 (DR1) main catalogue IDs of the analysed point sources

main source(s)	1eRASS
WR 22 (HD 92740)	J104117.5-594036
Cl* Collinder 228 TM 103	J104246.5-601209
WR 24 (HD 93131)	J104352.3-600704
HD 93129 + HD 93128	J104356.9-593252
HD 93160 + HD 93161	J104408.3-593432
WR 25 (HD 93162)	J104410.2-594310
HD 93206 (QZ Car)	J104422.8-595936
HD 93205 (V560 Car)	J104433.7-594412
HD 93250	J104445.0-593355
$\eta$ Car (HD 93308)	J104503.4-594103
HD 93403	J104544.0-592427